TIME-RESOLVED CHARACTERIZATION OF ULTRASHORT PULSE PROPAGATION

A Dissertation

by

MATTHEW MURRAY SPRINGER

Submitted to the Office of Graduate and Professional Studies of
Texas A&M University
in partial fulfillment of the requirements for the degree of

DOCTOR OF PHILOSOPHY

Chair of Committee,	Alexei V. Sokolov
Committee Members,	George W. Kattawar
	Edward S. Fry
	Phillip R. Hemmer
Head of Department,	George R. Welch

December 2013

Major Subject: Physics

ABSTRACT

The propagation of ultrashort femtosecond laser pulses in linear dielectric materials is determined in the time, space, and frequency domains by linear Maxwell optics through dispersion and diffraction. For intense pulses, pulse propagation is additionally modified by nonlinearities in the medium such as the optical Kerr effect, plasma generation, and self-phase modulation.

In this work we report the results of several experiments on the propagation of ultrashort pulses. In the linear regime, we characterize the temporal evolution of an ultrashort pulse during propagation through a linear dielectric under anomalous dispersion. Under these conditions the pulse evolution departs from the group velocity and group delay dispersion approximations, which leads to the formation of optical precursors. We describe an experiment which observes the propagation of optical precursors in a bulk condensed-matter dielectric. We generate ultrashort laser pulses and propagate the pulses through a bulk dye with an absorption resonance turned to the center wavelength of the femotsecond pulse. The pulse is then characterized in the time domain before and after propagation. Through numerical simulation we verify that the behavior of the precursors in the temporal pulse profile corresponds with the classical model.

Under very high intensity laser pulses, the nonlinearities induced by the propagation of the intense ultrashort pulse produce changes in the complex refractive index of the nonlinear material. We report the results of experiments involving time-resolved imaging of the propagation of ultrashort pulses in dielectric materials. We experimentally observe and characterize these effects through a weak-probe imaging effect which directly measures the nonlinearity in a time-resolved manner. In these

experiments an intense femtosecond laser pulse is propagated in a nonlinear intensity regime while an unfocused low-intensity femtosecond pulse is used as to probe the nonlinear pulse. We use this technique to characterize femtosecond pulses in air and liquid, especially in the regime of optical filamentation. We subsequently calculate parameters such as the plasma density, the transverse extent, and the instantaneous refractive index within the femtosecond laser filament under conditions which are not accessible through most standard pulse measurement techniques.

DEDICATION

To Briana, whose tireless and loving support has enriched my life immeasurably.

ACKNOWLEDGMENTS

Like all science, this work could not have existed without the help and support of numerous friends and colleagues. Their aid and advice has taught me all I know.

My advisor Alexei Sokolov has been the best mentor a student could possibly ask for. His patience, knowledge, and support have been more valuable than I can possibly describe adequately.

The optics group at Texas A&M University is certainly one of the most distinguished and productive groups in what is already one of the best physics departments in the country. George Kattawar in particular was the first professor I met during a tour as an undergrad, the first professor whose grants funded me on a joint project with Dr. Sokolov, and the professor who suggested my application for the SMART program which lead to my post-graduation employment. Marlan Scully has inspired and challenged me as the undisputed master of his subject, and I owe him special thanks for inviting me and many others to his incredible summer schools on quantum optics in the beautiful state of Wyoming. Ed Fry, George Welch, Alexander Kolomenski, and Hans Schusseler have all been a particularly fine set of colleagues. Without them this department would be a much poorer place.

Many graduates and postdocs have spent long days and nights in the lab with me helping make these and other results possible. Ben Strycker in particular has been a fantastic coworker, and our joint papers are a great source of pride. Life in a basement lab would not be nearly so enjoyable without the work and friendship of him and others including but certainly not limited to Charles Ballman, Kyle Damborsky, Francesco Echeverria, Ellie Figureoa, Brett Hokr, Dawson Nodurft, Chris O'Brien, James Strohaber, Jonathan Thompson, Andrew Traverso, Dimitri Voronine, Kai

Wang, Wenlong Yang, Zhenhuan Yi, and Miaochan Zhi. We do science and have fun doing it, and that's no small feat.

I also acknowledge those who have enriched my life outside the milieu of graduate life: my old college friends Aaron Lancaster and Michael Carney, my even older high school friends Chris Hertlein and Tyler Nezat, my high school teacher Dan McClellan, my siblings Laura and Mark, my parents John and Evodna, and my wife Briana. There are many others.

Money is a conserved quantity, and I gratefully acknowledge the support of various sources of funding including Texas A&M University, the US Office of Naval Research, the Welch Foundation, and especially the SMART Fellowship program and senior intelligence officer Forrest Cargile. Most of these directly or indirectly involve taxpayer money, and I promise to do my best to make their investment worthwhile.

> In whatever manner God created the world, it would always have been regular and in a certain general order. God, however, has chosen the most perfect, that is to say, the one which is at the same time the simplest in hypothesis and the richest in phenomena.
>
> Gottfried Leibniz, *Discours de Métaphysique*

I am thus finally grateful that we have been given such a universe to explore.

TABLE OF CONTENTS

LIST OF FIGURES

FIGURE Page

LIST OF TABLES

TABLE Page

1. INTRODUCTION TO ULTRASHORT PULSE PROPAGATION

1.1 Conceptual Framework

The present work is a study of ultrashort propagation in the linear and nonlinear regimes. In the linear regime, we study optical precursors. In the nonlinear regime, which comprises the bulk of this material, we use a time-resolved imaging technique to examine pulse propagation directly. Chapter 1 gives theoretical background for pulse propagation under both linear and nonlinear conditions, while the remainder of the text describes a number of experiments characterizing pulse propagation in these regimes.

As a matter of first principles, classical linear beam propagation has in principle been a solved problem since the work of James Clerk Maxwell in the 1860s [2]. While nominally Maxwell's equations are completely sufficient to understand ultrashort pulse propagation in the linear regime, there was little point in developing them into a comprehensive framework for describing the behavior of ultrashort pulses in dispersive media until the subject of optics matured in two directions, one theoretical and one experimental. In the theoretical realm, Einstein's theory of special relativity [3] sparked vigorous discussion on the questions of the meaning of group velocities or phase velocities which exceed c. Later, in the experimental realm, the development of pulsed electromagnetic sources such as mode-locked lasers allowed these theories to be directly tested and extended. Linear dispersion, while purely classical and independent of intensity, is enough to produce interesting phenomena such as optical precursors. The theory of optical precursors is reviewed in section 1.2.1, while our experiment involving measurement of optical precursors in a sharply absorbing dye is described in chapter 2.

The development of the theory of the laser [4] and the construction of a physical laser device [5] in the 1960s immediately resulted in light sources of extremely high intensity and opened the field of pulse propagation under the conditions of nonlinear optics. The extremely intense beams resulting from even continuous-wave (CW) laser processes were superseded in the intensity regime by the advent of q-switching and eventually mode-locking. The development of chirped pulse amplification (CPA) systems has resulted in the generation of femtosecond pulses with millijoules of energy. Instantaneous powers in the range of $10^{10}-10^{13}$ W and beyond are regularly achieved. Focused to the Gaussian limit of classical optics, this can lead to intensities greater than $10^{18}\,\mathrm{W/cm^2}$ in tabletop systems. Such intensities greatly modify the spatial and temporal dynamics of pulse propagation, leading to such phenomena as femtosecond laser filamentation. The theory of nonlinear pulse propagation and filamentation is reviewed in section 1.2.5. A method for the time-resolved imaging of femtosecond laser pulse nonlinearities including filamentation, along with the results of experiments involving this method, are described in chapters 3, 4, and 5.

1.2 Theoretical Review

1.2.1 Classical Pulse Propagation

The classical electromagnetic theory of Maxwell leads to the wave equation

$$\nabla^2\mathbf{E} - \mu\epsilon\frac{\partial^2}{\partial t^2}\mathbf{E} = 0, \tag{1.1}$$

shown here for the electric field $\mathbf{E}$ but equally valid for the magnetic field $\mathbf{B}$. This wave equation allows basic plane wave solutions of the form

$$E(\mathbf{r},t) = E_0 e^{i(\mathbf{k}\cdot\mathbf{r}-\omega t)}, \tag{1.2}$$

where ω is the angular frequency and $\mathbf{k}$ is a vector pointing in the direction of propagation of the wave with magnitude $k = \frac{2\pi}{\lambda}$, where λ is the wavelength. The wave equation is linear, so superpositions of solutions are themselves solutions. Each frequency component of the superposition is specified by its magnitude and phase, which may be described with a complex electric field amplitude $A(\omega)$. An arbitrary pulse in one dimension is thus described by an integral over all the frequency components:

$$E(x,t) = \int_{-\infty}^{\infty} \left[A(\omega)e^{i(\omega/c)n(\omega)x} + B(\omega)e^{-i(\omega/c)n(\omega)x}\right] e^{-i\omega t}\, d\omega, \tag{1.3}$$

where the frequency amplitudes $A(\omega)$ and $B(\omega)$ are given by

$$\left\{\begin{matrix} A(\omega) \\ B(\omega) \end{matrix}\right\} = \frac{1}{2}\frac{1}{2\pi}\int_{-\infty}^{\infty} \left[E(0,t) \mp \frac{ic}{\omega n(\omega)}\frac{\partial E}{\partial x}(0,t)\right] e^{i\omega t}\, dt. \tag{1.4}$$

In principle, once $A(\omega)$ and $B(\omega)$ have been calculated for the initial pulse, equation 1.3 completely reduces the problem of pulse propagation in a linear, homogeneous dielectric to the calculation of an integral.

However, the relationship between ω and k has been left unspecified. In general one is a function of the other. In this work we will treat ω as an independently variable parameter and $k(\omega)$ as the dependent variable. This choice is useful for calculating the shape of a pulse in time at a fixed position. The choice to treat ω as a function of k would be more useful for calculating the shape of a pulse in space at a fixed instant of time, and also make it somewhat easier to calculate the phase velocity $v_p = \omega/k$ and group velocity $v_g = \frac{d\omega}{dk}$. Propagation length within a sample of dielectric is usually the experimentally controllable parameter in these experiments, so we make the $k(\omega)$ choice despite the disadvantage in calculating velocity.

In vacuum, frequency and wavelength are straightforwardly related by $c = \omega/k$.

Each component propagates at the same phase velocity c and the pulse retains its shape and propagates distortion-free. In a dielectric, the relationship between the wavelength and frequency varies with the material properties of permittivity and permeability. These can be described with a single complex refractive index[1] whose real part relates the wavelength and frequency via

$$k = n(\omega)\frac{\omega}{c}. \tag{1.5}$$

In general the refractive index is a rank-2 tensor mapping the wavevector and position vector onto a complex scalar. However at this point we are assuming that the dielectric is isotropic and homogeneous, allowing us to replace $\mathbf{k} \cdot \mathbf{r}$ with kx, where x is defined along the direction of propagation. The superposition may be written as

$$E(x,t) = \int_{-\infty}^{\infty} A(\omega) e^{i(\tilde{n}(\omega)\frac{\omega}{c}x - \omega t)}\, d\omega. \tag{1.6}$$

Here $\tilde{n}(\omega)$ may be complex, and from equation 1.6 the real part is proportional to the phase shift per propagation distance while the imaginary part is related to the absorption per propagation distance.

Maxwell's equations do not independently constrain the allowed values of the refractive index as a function of frequency. In principle the refractive index can be less than 1, leading to phase velocities greater than c. The group velocity[2] may also be greater than c. Both may be greater than c simultaneously.

[1]The complex refractive index will always be denoted by $\tilde{n}(\omega)$ in this work. The real part will be denoted $n(\omega)$ or $n_R(\omega)$ as context requires. The imaginary part will always be denoted $n_I(\omega)$ when referred to explicitly.

[2]Identification of the group velocity with the "information velocity" is not uncommon. This is a good approximation in many practical situations such as the transmission of discrete pulses of light through a normally dispersive fiber optic communication link. However, it is certainly not true in general.

If we make the physically reasonable assumption that the polarization inducted in a linear dielectric at some instant depends only on the electric field experienced by the material at earlier times—i.e.,, that the medium is causal—the impulse response can be written as

$$P(t) = \epsilon_0 \int_{-\infty}^{t} \chi_T(t - t')E(t')\, dt', \tag{1.7}$$

where $\chi_T(t)$ is the time-domain electric susceptibility. If we take the Fourier transform of equation 1.7, the convolution theorem immediately implies that

$$P(\omega) = \epsilon_0 \chi(\omega) E(\omega). \tag{1.8}$$

Following the treatment of Byron and Fuller [6], consider the Fourier transform of $\chi(t)$ directly, using z to denote that we will extend this to the complex plane:

$$\chi(z) = \frac{1}{\sqrt{2\pi}} \int_{0}^{\infty} \chi_T(t) e^{izt}\, dt. \tag{1.9}$$

Due to the causal nature of the impulse response, the integral is evaluated from 0 to ∞. This Fourier transform may be expressed in terms of real and imaginary parts explicitly by the replacement $z = \omega + i\omega'$. This gives

$$\chi(z) = \frac{1}{\sqrt{2\pi}} \int_{0}^{\infty} \chi_T(t) e^{i\omega t} e^{-\omega' t}\, dt. \tag{1.10}$$

Provided that $\chi_T(t)$ is bounded, absolutely integrable, and equal to 0 for all $t < 0$, the function $\chi(z)$ defined in equation 1.10 is analytic in the upper half of the complex plane ($\omega' > 0$) because t is non-negative and the exponential term with the real argument is decaying. Because $\chi(z)$ is analytic in the upper half-plane and $|\chi(z)| \to 0$ as $|z| \to \infty$ in this region, its real and imaginary parts are Hilbert transforms of each

other (This identity is derived in detail in [6]):

$$\begin{aligned}\chi_R(\omega) &= \frac{1}{\pi}\mathrm{P}\int_{-\infty}^{\infty}\frac{\chi_I(\bar{\omega})}{\bar{\omega}-\omega}\,d\bar{\omega} \\ \chi_I(\omega) &= -\frac{1}{\pi}\mathrm{P}\int_{-\infty}^{\infty}\frac{\chi_R(\bar{\omega})}{\bar{\omega}-\omega}\,d\bar{\omega},\end{aligned} \tag{1.11}$$

where P denotes the Cauchy principle value. Because $\chi_T(t)$ is real, these may be rewritten in a more physically useful form involving only the positive frequency components:

$$\begin{aligned}\chi_R(\omega) &= \frac{2}{\pi}\mathrm{P}\int_{0}^{\infty}\frac{\bar{\omega}\chi_I(\bar{\omega})}{\bar{\omega}^2-\omega^2}\,d\bar{\omega} \\ \chi_I(\omega) &= -\frac{2\omega}{\pi}\mathrm{P}\int_{0}^{\infty}\frac{\chi_R(\bar{\omega})}{\bar{\omega}^2-\omega^2}\,d\bar{\omega}.\end{aligned} \tag{1.12}$$

These are the Kramers-Kronig relations, which relate the real and imaginary parts of the electric susceptibility under the assumption of causality. Unfortunately the complex refractive index $\tilde{n}(z) = \sqrt{1+\chi(z)}$ does not satisfy $|\tilde{n}(z)| \to 0$ as $|z| \to \infty$, so its real and imaginary parts are not related by equation 1.12. However, the real and imaginary parts of the refractive index do satisfy a suitably modified Kramers-Kronig relation. (This is also derived in detail in [6].) The result is

$$\begin{aligned}n_R(\omega) &= 1 + \frac{2}{\pi}\mathrm{P}\int_{0}^{\infty}\frac{\bar{\omega}n_I(\bar{\omega})}{\bar{\omega}^2-\omega^2}\,d\bar{\omega} \\ n_I(\omega) &= -\frac{2\omega}{\pi}\mathrm{P}\int_{0}^{\infty}\frac{n_R(\bar{\omega})}{\bar{\omega}^2-\omega^2}\,d\bar{\omega}.\end{aligned} \tag{1.13}$$

Equation 1.13 is a crucial result in the theory of causal pulse propagation. It shows that the real refractive index which describes phase velocity is not independent of the imaginary part which describes absorption. Each real refractive index curve is uniquely associated with an absorption spectrum, and this relation is enforced by

the requirement that the dielectric responds in a causal manner.

The most simple physically relevant causal model for the refractive index is the Lorentz oscillator model, where the molecules of the dielectric are modeled as classical damped driven harmonic oscillators. In the Lorentz model the dielectric permittivity is given by

$$\epsilon(\omega) = \epsilon_0 \left(1 + \left(\frac{Ne^2}{m\epsilon_0}\right) \frac{1}{\omega_0^2 - \omega^2 - 2i\gamma\omega}\right), \tag{1.14}$$

Where N is the number density, ω_0 is the resonance frequency, and γ is the damping parameter. The refractive index is then just $\tilde{n}(\omega) = \sqrt{\epsilon(\omega)/\epsilon_0}$, or

$$\tilde{n}(\omega) = \sqrt{1 + \left(\frac{Ne^2}{m\epsilon_0}\right) \frac{1}{\omega_0^2 - \omega^2 - 2i\gamma\omega}}. \tag{1.15}$$

As a conceptual exercise, consider equation 1.15 with all constants dimensionless and set to 1, except for $\omega_0 = 10$. The real and imaginary parts of the associated complex refractive index are shown in figures 1.1 and 1.2. Away from the absorption

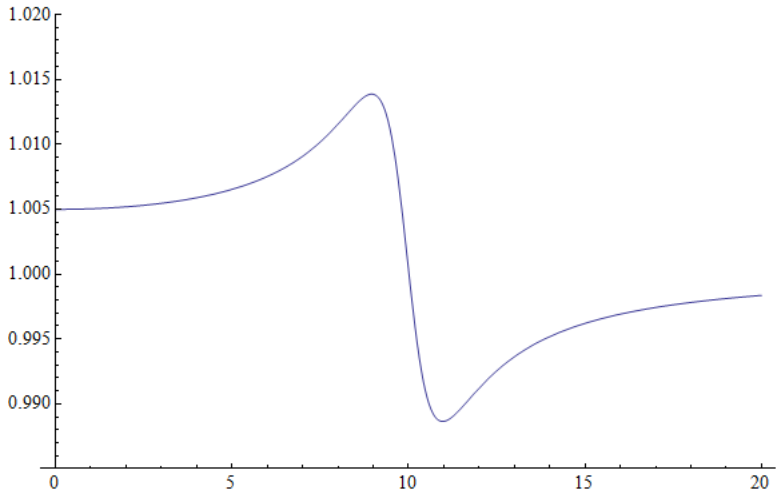

Figure 1.1: Real part of refractive index

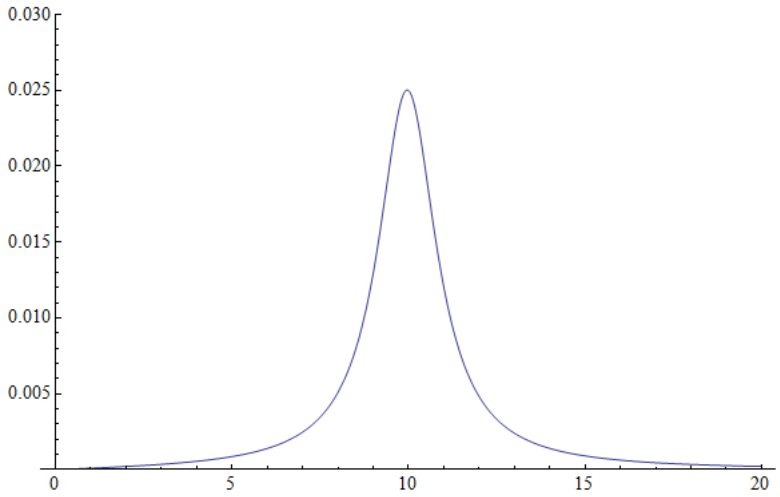

Figure 1.2: Imaginary part of refractive index

resonance, the real refractive index is increasing as a function of frequency. This is termed normal dispersion, and is responsible for phenomena such as the higher refractive index of glass at blue wavelengths as compared to red wavelengths. Near the absorption resonance, the real refractive index decreases as a function of frequency. This is termed anomalous dispersion. For frequencies greater than the resonance frequency the phase velocity exceeds c. The group velocity $v_g = \frac{d\omega}{dk} = \frac{c}{n+\frac{dn}{d\omega}}$ also exceeds c over the region of anomalous dispersion. While we know that the Lorentz model is causal because it satisfies the Kramers-Kronig relations, it is not immediately clear how the fact of causality can be reconciled with the greater-than-c phase and group velocities. This seeming inconsistency led to the development of the theory of optical precursors.

1.2.2 Optical Precursors

The time-domain amplitude of the electric field in equation 1.6 is a superposition of frequency components whose phases propagate with different velocities. For

convenience consider equation 1.6 written in terms of $\phi(\omega) = (k(\omega)x - \omega t)$,

$$E(x,t) = \int_{-\infty}^{\infty} A(\omega) e^{i\phi(\omega)}\, d\omega. \tag{1.16}$$

Following [7], we notice that the complex amplitude $A(\omega)$ (equation 1.4) is analytic in the upper half of the complex plane provided only that the electric field has a well-defined front $E(0,t) = 0$ for $t < 0$. If we integrate 1.16 over the upper half of the complex plane (i.e., $(x - ct > 0)$) via a closed contour which follows the real line and a semicircle of radius $|\omega| \to \infty$, Cauchy's theorem ensures that the integral will evaluate to 0 because $A(\omega)$ and $k(\omega)$ are analytic within the enclosed region. However, the integral along the semicircular contour is separately 0 in view of the fact that $k(\omega)$ goes to $\frac{\omega}{c}$ for large $|\omega|$ in the upper half plane, and thus e^{ikx} goes to $e^{i\frac{\omega x}{c}}$ which approaches 0 for large $|\omega|$.

Given that the upper portion of the contour integrates to zero, the lower part of the contour along the real axis must also be zero. Thus for any initial pulse which a sharp leading edge, no signal can propagate faster than c.

Having shown that the propagation of a pulse front occurs at a velocity below the vacuum speed of light, we can now examine the development of the pulse behind the propagating front. An extremely comprehensive and sophisticated treatment is found in [8], but here we continue to follow the conceptually simpler argument of [7]. Since the exponential term of equation 1.16 is oscillatory, the most important contribution to the integral occur at the points of stationary phase where $\partial\phi/\partial\omega = 0$. This occurs at

$$n(\omega) + \omega \frac{\partial n(\omega)}{\partial \omega} = \frac{t}{t_0}, \tag{1.17}$$

where $t_0 = x/c$. At very high frequencies the left hand side of equation 1.17 ap-

proaches 1, showing that the leading edge of the pulse will be a high-frequency, low-amplitude component beginning immediately when $t > t_0$. This is the Sommerfeld precursor. Another precursor is associated with the $\omega = 0$. For this Brillouin precursor, the associated frequency is lower and its timing is set by the point where $t/t_0 = n(0)$. The subsequent evolution of the pulse is eventually determined by the form of the individual pulse.

Aside from the fact that they need not and generally do not propagate at the group velocity, optical precursors have a number of interesting properties. Among these is the fact that precursors do not attenuate exponentially with propagation distance in an absorbing medium. While each frequency component is individually attenuated in the usual exponential way due under linear propagation, the time-domain precursors can "leach" energy from the main part of the pulse and maintain their amplitudes over longer propagation distances. The total energy of the precursors and main pulse attenuate exponentially in the usual way as well.

1.2.3 Classical Beam Propagation

The development of classical electromagnetism by Maxwell led to a comprehensive framework of describing the propagation of light. The Maxwellian theory of electromagnetism includes solutions satisfying the vector wave equation 1.1. In free space the values of the permittivity and permeability are constant and lead to a wave speed $c = 1/\sqrt{\mu_0\epsilon_0} = 2.99 \times 10^8\,\mathrm{m/s}$. In dielectric materials the permittivity ϵ and permeability μ vary from material to material and are functions of the frequency of the propagating electromagnetic fields. This dependence of the phase velocity $v_p = 1/\sqrt{\mu(\omega)\epsilon(\omega)} \equiv c/n(\omega)$ of light in a material medium defines the real refractive index $n(\omega)$.

Given boundaries and initial conditions, full solutions may be built up from

Fourier superpositions of these basic plane wave solutions, each with their own $E_0(\mathbf{r}, t)$. In laser physics it is generally reasonable to define a axis of propagation z along the beam. If the divergence of the beam is not too high, we may plug 1.2 into 1.1 and the small divergence angle justifies dropping terms in $\frac{\partial^2}{\partial z^2}$. Details of the calculation may be found in [9] or other standard references. The result is the familiar paraxial approximation to the Helmholtz equation:

$$\nabla_\perp^2 E_0 + 2ik\frac{\partial E_0}{\partial z} = 0. \tag{1.18}$$

The paraxial wave equation supports several families of solutions depending on the choice of coordinates. Cylindrical symmetry is a natural choice for laser beam propagation, and leads to the Laguerre-Gauss modes. The lowest-order mode—the TEM_{00} mode—is both the most common choice for laser resonators and the "minimum uncertainty" mode in terms of the product of divergence angle and focal spot size. Its functional form is

$$E(r, z) = E_0\frac{w_0}{w(z)}\exp\left(\frac{-r^2}{w^2(z)} + ikz + ik\frac{r^2}{2R(z)} - i\zeta(z)\right), \tag{1.19}$$

where $w(z)$ is the transverse extent of the beams in terms of $1/e$ falloff in electric field amplitude, $R(z)$ is the radius of curvature, and $\zeta(z)$ is the Gouy phase $\zeta(z) = \arctan\left(\frac{z}{z_\mathrm{R}}\right)$ where we further define the Rayleigh range $z_\mathrm{R} = \frac{\pi w_0^2}{\lambda}$. This leads to the inverse relationship between the beam divergence angle and the size of the focal spot:

$$\theta = \frac{\lambda}{\pi w_0}. \tag{1.20}$$

Note that θ is the angle with respect to the z axis of propagation. The divergence of the beam as a whole is $\Theta = 2\theta$. As such a classical beam is fundamentally limited in

that the product of its waist size and divergence angle cannot become smaller than approximately λ. If the waist-angle product of a beam is substantially smaller than the wavelength, this is a clear indication of non-classical beam propagation. However, a beam may propagate non-classically without breaking the $\theta w_0 \gtrsim \lambda$ product—one example is plasma generation with defocusing which makes the beam waist much wider than classically expected. An experiment involving this form of nonclassical propagation is discussed in chapter 3.

1.2.4 Nonlinear Optics: Self-Focusing

The classical Maxwell description of the propagation of electromagnetic waves generally assumes that the response of the material to the electromagnetic field is linear in the field strength. Such an assumption is generally reasonable for field strengths much lower than the typical intra-atomic fields on the order of $5 \times 10^{11}\,\mathrm{V/m}$, which is generally true for common sources such as sunlight, indoor lighting, etc. Higher intensities lead to numerous novel effects including nonlinear index of refraction in which the refractive index is modulated by the incident beam according to

$$n = n_0 + n_2 I \tag{1.21}$$

for the time-averaged intensity $I = 2n_0\epsilon_0 c|E(\omega)|^2$. In air, $n_2 = 5.0 \times 10^{19}\,\mathrm{cm^2/W}$ while for liquid water $n_2 = 4.1 \times 10^{16}\,\mathrm{cm^2/W}$ is a typical value [1].

In 1.2.3 we found that Gaussian beams do not have an intensity which is constant over their cross-sections. Instead, the beam intensity is a Gaussian function of the distance from the propagation axis. If the beam intensity is sufficient, this spatial variation of the intensity results in a spatial variation of the refractive index through the nonlinear response of the medium. An enhanced refractive index near the center is effectively the definition of a gradient-index lens, and self-focusing becomes possible.

This immediately suggests the possibility that the diffraction inherent in Gaussian beams could be balanced by self-focusing, resulting in a self-trapped beam. For pulses of finite duration, this suggests the possibility of soliton behavior.

To explore this possibility, we follow the treatments of [9, 10] and begin with the nonlinear Schrodinger equation

$$\nabla_{\perp}^2 E_0 + 2ik\frac{\partial E_0}{\partial z} + \frac{k^2 n_2}{n_0}|E_0|^2 E_0 = 0, \tag{1.22}$$

which is just the paraxial wave equation with an additional intensity-dependent term which models the nonlinear refractive index. The diffraction is driven by the transverse Laplacian term while the self-focusing is driven by the intensity term $|E_0|^2$. Should these terms happen to be comparable in magnitude we would have an estimate for the range of parameters in which self-trapping might be possible. Given some typical beam radius a_0, we seek the intensity where $a_0^2|E_0|^2 \sim \frac{n_0}{k^2 n_0}$. Solving, we find that the a_0 term drops out (diffraction and intensity both scale with beam size) and we have a *critical power*

$$\mathrm{P_{cr}} \sim \frac{\lambda^2}{2\pi n_0 n_2}. \tag{1.23}$$

For 800 nm lasers in air, the critical power is on the order of 2.4 GW. For fused silica, the critical power is around 1.6 MW. This suggests that a true balance between self-focusing and diffraction might be achievable with power levels typical of pulsed laser systems. While there is such a power level, the balance turns out not to be stable. A static balance between diffraction and self-focusing would be an example of a two-dimensional spatial soliton, and these are known to be unstable in the general case [1, 11, 12].

Material	n_0	n_2 (cm^2/W)
BK-7 glass	1.52	3.4×10^{-16}
Water	1.33	4.1×10^{-16}
Air	1.0003	5.0×10^{-19}

Table 1.1: Nonlinear index of refraction for various typical materials: solid, liquid, gas (from [1])

1.2.5 Filamentation: Balance of Self-Focusing and Defocusing

In the previous section we calculated that there exists a critical power at which diffractive spreading and self-focusing are in balance. This equilibrium is not stable. Below the critical power, diffraction will cause the beam to spread. Above the critical power, self-focusing will cause the beam to collapse. During the collapse process, the intensity will increase such that the intensity-proportional nonlinear refractive index model $n = n_0 + n_2 I$ loses its validity and higher-order terms become relevant. These terms cause the pulse to defocus and serve to arrest the collapse. The primary defocusing term originates from free electron plasma created by ionization at high intensity.

Following the notation of [13], the change in the refractive index due to the generation of plasma is

$$\Delta n_p = -\frac{\omega_p^2}{2\omega_0^2}, \tag{1.24}$$

where ω_0 is the frequency of the laser pulse and the plasma frequency ω_p is given by

$$\omega_p = \sqrt{\frac{e^2}{\epsilon_0 m_e} N_e}. \tag{1.25}$$

In equation 1.25, N_e is the number density of electrons. In the photon picture, a laser pulse of 800 nm will have an energy of 1.55 eV. According to [14], the ionization

energy of N_2 is about 15.57 eV and that of O_2 is about 12.06 eV. This suggests that about 8 photons will be required to begin ionizing air. An 8-photon process is expected to scale with intensity at about the I^8 level. In the subsequent discussion we will leave the specific ratio unspecified and assume that plasma generation scales with I^m. Combining 1.24 and 1.25, the overall refractive index is thus given by

$$n = n_0 + n_2 I - \frac{e^2}{2\epsilon_0 m_e \omega_0^2} \beta I^m, \tag{1.26}$$

where β gives the scale of the plasma generation in the particular medium. For very low intensity, the overall propagation is linear and n is constant. For higher intensity, the term proportional to I dominates and self-focusing occurs. As self-focusing proceeds, the I^m plasma defocusing term increases until it balances the self-focusing term. The critical intensity at which this occurs varies according to the specific properties of the material in question, but for air is on the order of $4 \times 10^{13}\,\mathrm{W/cm^2}$ [15]. For a pulse with a given peak power, the critical intensity sets the transverse size of the resulting filament. In air this size is typically on the order of 100 microns; in condensed matter the size is on the order of 5 microns [16–19].

The density of plasma required to arrest self-focusing and set the critical intensity is quite low. Typically only on the number density of free electrons is on the order of 1% of the number density of molecules; in air the free electron number density is around $10^{16}\,\mathrm{cm^{-3}}$ [20–22].

Filamentation is not a phenomena with a universally accepted definition, and there are a number of propagation regimes which fit some authors' definitions but not others. Some authors (for instance, [23]) define filamentation in terms of the intensity clamping described in this section. Filamentation is also frequently described (for instance, by [24]) in terms of the pulse maintaining a small beam size

for a propagation distance which is longer than the classical linear Raleigh length described in section 1.2.3.

1.2.6 Filamentation: Self-Phase Modulation

One of the key diagnostic criteria for observing filamentation in practice is the generation of a broad supercontinuum of light which includes frequency content throughout the visible range. In equation 1.6, the phases of each frequency component of the wave are given by

$$\exp i\left(\frac{\omega n}{c}x\right). \tag{1.27}$$

In this case the refractive index n is implicitly constant in view of the linear nature of the propagation. During filamentation, the variation of the refractive index due to the intensity induces a change in phase given by

$$\Delta\omega = \frac{\omega}{c}x\frac{\partial\left[\Delta n(t)\right]}{\partial t}. \tag{1.28}$$

As discussed in section 1.2.5, the refractive index in filamentation is determined by competition between the Kerr effect and plasma defocusing. However, this competition is not a static balance. The leading portion of the pulse is below the instantaneous intensity required to generate plasma, and thus only experiences a $\Delta\omega$ which corresponds to the positive change in index. This leads to a shift toward the low-frequency end of the spectrum. For the central and trailing of the pulse, the sign of the self-phase modulation is reversed within the plasma and as the intensity decreases with time, leading to a blue shift. In combination these processes lead to a broadening of the spectrum of the pulse.

Thus far we have treated the pulse in an essentially one-dimensional manner.

However, the filament is not a plane wave and in general a 3+1 dimensional treatment of the problem is required, which contributes to the difficulty of accurately simulating the propagation of filaments. Self-phase modulation in the radial direction results in conical emission, the angle-dependence of the self-phase-modulated radiation [25]. Again following [13], the wave vector representing the light at each point along the pulse front is

$$\vec{k} = k_x\hat{x} + k_r\hat{r} = \Delta k_x\hat{x} + k_{r0}\hat{r} + \Delta k_r\hat{r}. \tag{1.29}$$

The change in the z component of the wavevector is given by

$$\Delta k_x\hat{x} = \frac{\omega\Delta n}{c}\hat{x}. \tag{1.30}$$

Recognizing that $x = ct$, this becomes equal to

$$\Delta k_x\hat{x} = \frac{\omega}{c}n_2\int_0^x \frac{\partial I_{front}}{\partial t}\,dx\,\hat{x} - \frac{e^2}{2\epsilon_0 c m_e\omega}\int_0^x \frac{\partial N_e}{\partial t}\,dx\,\hat{x}. \tag{1.31}$$

For the section of the pulse which contains the highest intensity and thus the highest plasma concentration, this quantity is negative. For the leading part of the pulse which is in the non-ionized part of the dielectric, this is positive. Given that k has components in the $\hat{x}$ and $\hat{r}$ directions, a change in k_x will necessarily result in a change in the transverse part of the wave vector k_r. This self-phase modulation in the radial direction is the origin of the conical emission which is characteristic of optical filamentation, and is among the useful characteristics of filaments for remote sensing [26].

1.2.7 Filamentation: Beam Breakup

Optical filaments with a peak instantaneous power much greater than the critical power, $P \gg P_{cr}$, do not form single filaments with very large diameters which surround a core with an intensity of magnitude equal to the critical intensity. Instead, the beam develops instabilities which lead to the breakup of the beam into individual filaments which share a common energy reservoir halo. Each individual filament has a peak power $P \approx P_{cr}$ and a transverse diameter comparable to an isolated individual filament.

Beginning with the nonlinear Schrodinger equation 1.22 and following the treatment and notation of Boyd [1], we can write the expression which governs the propagation of the pulse

$$2ik\frac{\partial E_0}{\partial x} + \nabla_\perp^2 E_0 = -\frac{\omega^2}{\epsilon_0 c^2} p_0. \tag{1.32}$$

The transverse Laplacian of the central part of the pulse E_0 is equal to 0, and thus

$$E_0(x) = A_{00} e^{i\gamma x}. \tag{1.33}$$

The scale factor in the exponential term gives the strength of the nonlinear phase accumulation, $\gamma = n_2 k_{vac} I$. The side modes $E_\pm$ are coupled to the nonlinear polarization via

$$p_{\pm 1} = 3\epsilon_0 \chi^{(3)} \left[2|E_{00}|^2 E_\pm + E_{00}^2 e^{2i\gamma x} E_\mp^* \right]. \tag{1.34}$$

Introducing the definition $E_\pm = a_\pm e^{i\mathbf{q}\cdot\mathbf{r}}$, the differential equation 1.22 and the polarization coupling expression 1.34 set the propagation is

$$2ik\frac{\partial a_{\pm 1}}{\partial x} - q^2 a_{\pm 1} = -\frac{\omega^2}{c^2} 3\chi^{(3)} |E_{00}|^2 \left[2a_{\pm 1} + a_\mp^* e^{2i\gamma x} \right]. \tag{1.35}$$

The solution is straightforward if slightly tedious. Boyd makes the substitution $a_{\pm 1} = a'_{\pm 1} e^{i\gamma x}$ and seeks a solution of the form

$$\begin{bmatrix} a(x) \\ a^*(x) \end{bmatrix} = \begin{bmatrix} a(0) \\ a^*(0) \end{bmatrix} e^{\Lambda x}, \tag{1.36}$$

These equations have such a solution solution where $\Lambda = \pm\sqrt{\beta(2\gamma - \beta)}$, where $\beta = q^2/2k$. Here gain is possible where $\gamma > \frac{1}{2}\beta$. In this context gain is growth in the size modes at the expense of the main beam—this is effectively a simplified picture of beam breakup. The maximum wavevector at which gain is possible is $q_{max} = 2\sqrt{k\gamma}$ and the maximum gain is given by $q_{opt} = q_{max}/\sqrt{2}$, for an angle of maximum gain of $\theta_{opt} = q_{opt}/k$.

If we define the effective waist size defined by this side-mode gain, $w_{eff} = (\pi/q_{max})^2$, we can calculate the per-filament power. Since $q_{max} = 2\sqrt{k\gamma}$, and $\gamma = n_2 k_{vac} I$, we find that the per-filament power is

$$P_{fil} = \frac{\lambda^2}{8 n_0 n_2}. \tag{1.37}$$

Up to a constant this is the same as the critical power for self-focusing. In practice beam breakup is much more complicated, but this simple model demonstrates the possibility of beam breakup for high power pulses.

1.3 Literature Review

1.3.1 Optical Precursor Literature

After Einstein [3] constructed the theory of special relativity and established that causality prohibited causal contact between events separated by spacelike intervals ($c^2\Delta t^2 < \Delta r^2$). Since neither relativity nor Maxwell's equations restricted the phase

and group velocities within dielectric media to less than the vacuum speed of light, it was not immediately clear how linear optics and causality could be reconciled. In 1914, Sommerfeld [27] and Brillouin [28] developed the theory of optical precursors. The found that in the case of discontinuous pulse fronts and other types of non-analytic signals, the points where the pulse is non-analytic propagate via small precursor fields which arrive before the main signal. The first precursor is termed the Sommerfeld precursor, consists of the high-frequency components of the pulse, and travels at the vacuum speed of light. This is followed by the Brillouin precursor, which consists of the low-frequency components of the pulse. Following these precursor fields, the main signal arrives, possibly altered in amplitude and distorted by its passage through the dielectric. The Sommerfeld and Brillouin analysis indiecated that precursor fields were generally very small in amplitude, perhaps 10^{-7} times the integrated energy of the main pulse.

The mathematical description of precursors was extensively developed and clarified by Oughstun and Sherman, who additionally showed that the amplitude estimate of Sommerfeld and Brillouin was mistaken and that in fact precursor fields could become comparable in amplitude to the main pulse [8, 29, 30]. This opened the possibility of experimental observation of precursors.

Because optical precursors are inherently a relatively few-cycle phenomena, optical precursors were not a viable subject of experimental study and the early experimental work on precursors was conducted in the radio and microwave regimes. The first experimental observation was due to Pleshko and Palóz in 1969 [31], who conducted an experiment involving the propagation of microwaves in waveguides which were constructed to provide the appropriate dispersion characteristics. Additional work was conducted in superfluid ^{3}He, which has sonic dispersion characteristics analogous to a Lorentz medium [32]. Under these conditions of very low $\tilde{3}40$ m/s

wave velocity for the sound waves, time-resolved measurements of precursor phenomena were reasonably straightforward and in accordance with theoretical predictions. Precursors in the optical domain did not become accessible until the development of femtosecond laser pulses.

A number of efforts have been put forth to observe optical precursors. Many of the most successful efforts have utilized dispersive media with sharp absorption resonances in order to take advantage of the rapid variation of the index of refraction. In 2006, Jeong et. al. observed optical precursors formed in a pulse propagating through cold potassium vapor in a magneto-optical trap [33]. In this experiment the optical depth was small, less than or equal to approximately 1. Others extended this to atomic vapors of greater optical depth [34, 35]. Additional efforts in atomic vapors, for instance, toward enhanced precursor strength by propagation through gain media are detailed in the review by Chin [36].

In condensed matter the situation is more difficult due to the broader and less easily tailored absorption bands and dispersion curves. Aaviksoo and coworkers observed optical precursors in a thin film semiconductor GaAs [37]. In 2004, Choi and Österberg reported an experimental observation of non-exponential pulse attenuation in water, which they attributed to precursors. This provoked considerable commentary and discussion [38,39], which argued that the observations of Choi and Österberg were due to linear frequency-dependent absorption rather than optical precursor formation. Work at Texas A&M helped clarify the issue by examining both the linear propagation of shaped ultrashort pulses and the possibility of nonlinear spectral transformation in the water-propagating pulse [40,41]. Further experiments, described in the present work, have found indications of precursor behavior in liquid water [42].

1.3.2 Characterization of Femtosecond Laser Filaments

Though self-focusing and self-trapping had been predicted and observed long before [11, 43–45], the first experimental indication of femtosecond filamentation was observed by Braun [46]. It was observed that pulses of 200 fs duration and tens of mJ energy would spontaneously self-channel due to Kerr focusing and defocusing which Braun attributed to both diffraction and plasma generation. The characteristic white light conically emitted by the process of self-phase modulation was noted and characterized by Nibbering [47]. While the focus of the present work is primarily on the characterization of filament evolution via imaging, it is worthwhile to briefly give some examples of more general research directions of filamentation research.

The principle difficulty of measuring and characterizing filaments is their extreme intensity. In their comprehensive review article, Couarion and Mysyrowicz [16] note that filaments may occur in dielectrics of different phases and density (such as air and liquid water), with the central filament core typically reaching intensities of $10^{13} - 10^{14}\,\mathrm{W/cm^2}$. Traditional measurement techniques such as CCD beam profilers and time-domain measurement techniques such as autocorrelation and FROG[3] [48] are hampered in that they expose a solid nonlinear medium to intensities which result in the inevitable destruction of the measuring device.

While the $3+1$ dimensional nature of the problem complicates both theory and simulation, many groups have evaluated the nonlinear propagation of optical pulses under various circumstances. Feng gives a detailed overview of breakdown in water [49]. Tang has also provided a detailed theory of pump-probe experiments with chirped pulses in nonlinear media [50]. For the specific case of the ionization of air molecules involved in the plasma generation which plays an important role in

[3] and its colorfully-named variant techniques such as SPIDER, GRENOUILLE, TADPOLE, etc.

defocusing, Talebpour and coworkers have also provided a detailed semi-empirical description [14]. Kasperian and others in the Teramobile project conducted detailed work on the critical intensity for self-guided pulses in air [15].

Aside from imaging methods which we will review in section 1.3.3, a number of other methods have been developed for evaluation of filaments in the absence of the ability of expose traditional measuring devices directly to the filament. One alternative is to use the damage track itself to characterize the filament [17–19,51–53]. This method has the disadvantages of not being time resolved, lack of dynamic range in intensity, and the single-shot nature of the damage process. However, it is straightforward and inexpensive.

Relatively simple characterizations based on non-time-resolved observation of the generated white light have also been productive. Lange and collaborators experimentally investigated self-guiding vs. moving-focus models using light reflections from a mirror in a gas cell and found that their observations supported the self-guiding model [54]. LaFontaine used a long propagation length and a spectrometer and CCD to examine filament propagation over distance greater than 200 meters [20]. Liu used a similar method to explore the random deflection of pulses undergoing filamentation in water [55]. Others have used similar techniques [24, 56–59]. One particularly relevant work using this method is that of Hao [60], who examined beam breakup in free vs. prefocused propagation. A clever extension of these techniques to characterize pulses using FROG methods was conducted by Shulz [61] using a specially constructed argon cell.

The group of Tzortzakis and coworkers [21] take advantage of the fact that plasma is electrically conductive and are able to characterize plasma conductivity generated by the filament on nanosecond time scales. They also measure the filament with an all-optical diffractometry method. In the case of the Tzortzakis work, the filament is

generated by a 2 m focal length lens with 120 fs pulse length and 14 mJ energy, which is in the regime consistent with filamentation in the absence of optical breakdown [13, 16, 23].

The nonlinearities which drive filamentation result in a number of optical processes which emit light in directions away from the filament core. The fluorescence of the filament plasma has been directly imaged in a non-time-resolved fashion in a microscope objective [62–65]. Nguyen [66] used this method to characterize the competition between optical breakdown in filamentation, which we also explore in chapter 3. Theberge used a pump-probe version of this technique to measure the dependence of plasma density on external focusing [67].

The group of Yu and coworkers has engaged in sonographic probing of filaments [68]. In this work, the sounds generated by the expansion of the plasma in air were recorded directly by microphone and used to characterize the filament along its direction of propagation.

Filaments have been used to characterize other filaments, such as by crossing the filaments at differing delays and observing energy transfer both on the scale of the pulse [69, 70] and on interferometric scales [71].

1.3.3 Time-Resolved Imaging of Filaments

This present work involves the characterization of femtosecond laser filaments through time-resolved imaging, shadowgraphy, and birefringence mapping. Imaging of ultrafast nonlinear phenomena has long been used for the characterization of shock waves and bubble formation on nanosecond time scales [72–75] with more recent work on picosecond and femtosecond time scales [75, 76].

Several groups have used time-resolved shadowgraph techniques to probe ultrafast nonlinear optical phenomena. Fujumoto used time-resolved polarigraphic imag-

ing to examine the propagation of intense focused pulses in air [77, 78], as well as using imaging to examine the propagation of single pulses at various delays [79]. Abraham used shadowgraphy and interferometry to probe optical breakdown in water on femtosecond and picosecond time scales [80]. Rambo used an interferometric imaging technique which was sensitive to the time rate of change of the refractive index in pulses [81]. Rodriguez performed shadowgraphy on loosely-focused pulses in air to determined the plasma density [82]. Among the groups using holographic techniques are those of Balciunas [83] and Minardi [84, 85]. These techniques reveal information about the spatial distribution of the refractive index, but without direct imaging.

Mao directly imaged the propagation of a femtosecond laser plasma in a glass dielectric medium at various intensity levels and calculate the electron density [86]. Centurion also uses an instantaneous shadowgraph/holograph to image the generation of plasma from a tightly-focused pulse—we approach this problem using direct imaging in chapter 3 and also in the context of loosely-focused filaments outside the regime of optical breakdown chapter 5. Liu used a similar method to explore a more loosely-focused plasma generated by a 1 kHz laser, though in a non-time-resolved manner [87]. Hayasaki performed a similar measurement with low-energy pulses propagating in glass [88]. Gawelda [89] performed pump-probe microscopy of tightly-focused kHz pulses in glass, while Papazoglou [90] and Liu [91] performed similar work on very tightly-focused pulses in air. Another time-resolved palarigraphic method using supercontinuum as probe light was carried out by Yan [92] using relatively tightly-focused pulses in liquid CS_2.

2. OPTICAL PRECURSORS AND PULSE DISTORTION IN THE LINEAR PROPAGATION REGIME*

2.1 Introduction and Conceptual Structure

In linear propagation through a material, monochromatic light undergoes absorptive attenuation according to $I = I_0 e^{-x/d_a}$, where d_a is the attenuation length.* For continuous broad-spectrum light or ultrashort of broad bandwidth, each frequency component is attenuated exponentially at a characteristic frequency-dependent rate $I(\omega) = I_0(\omega)e^{-x/d_a(\omega)}$. Thus the total integrated energy of the pulse as a whole need not be attenuated according to a single clean exponential, but each frequency does obey this Bouger-Lambert-Beer (BLB) exponential attenuation on a frequency-by-frequency basis. It also trivially applies to the total energy of the pulse in the time domain.

It may be tempting to suppose that this BLB attenuation applies to each part of the pulse in the time domain as well. This would imply that each time-domain feature of a pulse attenuates with propagation distance at the same rate at the total integrated energy of the pulse, provided that the frequency content of the pulse is evenly distributed in the time domain[1]. For instance, the leading portion of the pulse would attenuate at the same rate as the pulse peak, which itself attenuates at the same rate as the integrated pulse as a whole. While this is a reasonable approximation in some common special cases, optical precursors do not attenuate at

*Portions of this chapter are reprinted with permission from material previously published in Matthew M. Springer, Wenlong Yang, Alexandre A. Kolomenski, Hans A. Schuessler, James Strohaber, George W. Kattawar, and Alexei V. Sokolov, Physical Review A (83), 043817, 2011. Copyright 2011 by the American Physical Society.

[1]I.e., an unchirped pulse as contrasted with a chirped pulse. However, the evolution of time-frequency representations of pulses (such as instantaneous frequency, spectrograms, and Wigner functions) during dispersive propagation is not trivial. In the case of precursors, for instance, frequency-domain attenuation does not correspond to time-domain attenuation.

the same rate as the entire pulse. In all cases, the pulse attenuates according to the BLB law on a frequency-by-frequency basis, but the BLB law alone is not sufficient to determine how the energy is distributed though the time domain within the pulse itself.

While optical precursors attenuate in a non-exponential manner [93, 94], non-exponential attenuation of the total pulse energy can also be a simple manifestation of the fact that each frequency component attenuates exponentially at an independent rate according to the BLB law. Thus the presence of optical precursors cannot be diagnosed solely by the non-exponential attenuation of the total pulse energy [40].

Direct observation of optical precursors thus requires characterization of the pulse in the time domain. Precursors involving RF pulses or optical pulses in specialized media have been directly observed and these experiments are discussed in section 1.3.1. This chapter describes the experiment published by the author and coworkers in [42,95], which experimentally characterizes precursor behavior of optical precursors in bulk condensed matter. We select an organic dye solution with a sharp absorption band near the center wavelength of our ultrafast laser, which additionally implies a sharply varying index of refraction through the Kramers-Kronig relationship in equation 1.13. The shape of the ultrafast pulse before and after the dye solution is characterized by an interferometric autocorrelator before and after the dye solution. This characterization of the pulse shape and its change after propagation through the absorptive and dispersive medium allows individual few-cycle pulse features to be tracked and their shape and attenuation individually characterized. The attenuation of some of these features at rates other than the attenuation rate of the overall pulse is indicative of precursor behavior.

2.2 Mathematical Framework

The frequency representation of a plane wave in one dimension is

$$A(\omega) = \frac{1}{\sqrt{2\pi}} \int_{-\infty}^{\infty} E(0,t) e^{i\omega t}\, dt, \tag{2.1}$$

provided that $\frac{\partial E}{\partial x}(0,t) = 0$, which assumes we are only interested in the forward-propagating part of the plane wave. (See the discussion in section 1.2.1 for further details.) The wave in the time domain representation is then a sum over these frequencies:

$$E(x,t) = \frac{1}{\sqrt{2\pi}} \int_{0}^{\infty} A(\omega) e^{i(\omega/c)\tilde{n}(\omega)x} e^{-i\omega t}\, d\omega + \text{c.c.}. \tag{2.2}$$

The evolution of the wave is controlled by the phase and amplitude changes introduced by the $i(\omega/c)\tilde{n}(\omega)x$ term as x increases during propagation. The refractive index $\tilde{n}(\omega) = n_R(\omega) + in_I(\omega)$ is divided into a real part which determines the rate of accumulation of phase with distance, and an imaginary part which determines the rate of attenuation or gain with distance. The distance attenuation coefficient $\alpha(\omega$ in the distance attenuation expression $I(\omega) = I_0(\omega) = e^{-\alpha(\omega)x}$ at a given frequency is thus related to the imaginary part of the refractive index by $n_I(\omega) = c\alpha(\omega)/2\omega$, where the factor of 2 results from the fact that intensity is proportional to the square of the field.

Thus in a linear, homogeneous, dielectric the evolution of a known pulse $A(\omega)$ reduces to the evaluation of an integral provided that the total refraction $\tilde{n}(\omega)x$ is known. In general the complex refractive index is not available in closed form for bulk dielectrics. However, the absorption spectrum is often experimentally easy to measure. The absorption spectrum is directly proportional to the imaginary part of the complex refractive index, and given the complex refractive index, the Kramers-

Kronig relations uniquely determine the real part of the index of refraction. From equation 1.13, the real part of the compex refractive index is related to the imaginary part by

$$n_R(\omega) = 1 + \frac{2}{\pi}\mathrm{P}\int_0^\infty \frac{\bar{\omega} n_I(\bar{\omega})}{\bar{\omega}^2 - \omega^2}\, d\bar{\omega}.$$

In principle complete knowledge of $n_I(\omega)$ over all frequencies is required to uniquely specify $n_R(\omega)$. However, the functional form of 1.13 ensures that for any given frequency ω_0, values of $n_I(\omega)$ where $|\omega^2 - \omega_0^2|$ is large will not contribute much to the integrand. Since optical precursors are determined largely by sharp gradients in the index of refraction, they will not be substantially affected by very these very high frequency values of $n_I(\omega)$ or the constant added to the real part of the refractive index by the low-frequency absorption $n_I(0)$.

For experiments such as this one where the propagation length is not accurately known, it is convenient to rewrite these relationships in terms of the optical depth $\tau(\omega) = \alpha(\omega)d$, where d is the total propagation length. In this case the Kramers-Kronig relationship is

$$n_R(\omega) = 1 + \frac{c}{\pi d}\mathrm{P}\int_0^\infty \frac{\tau(\bar{\omega})}{\bar{\omega}^2 - \omega^2}\, d\bar{\omega}. \tag{2.3}$$

In this notation, the coefficient $n_R(\omega)x$ for the phase shift is

$$n_R(\omega)x = x + \phi\frac{c}{\pi}\mathrm{P}\int_0^\infty \frac{\tau(\bar{\omega})}{\bar{\omega}^2 - \omega^2}\, d\bar{\omega}, \tag{2.4}$$

where we define the fractional propagation length $\phi = x/d$. One final notational simplification which is useful for obtaining numerical results is the definition of a total refraction

$$N(\omega)x = \frac{c}{\pi}\mathrm{P}\int_0^\infty \frac{\tau(\bar{\omega})}{\bar{\omega}^2 - \omega^2}\, d\bar{\omega}, \tag{2.5}$$

which can be used in calculating the relative phase shift $\frac{\omega}{c}N(\omega)\phi$. Using this notation, we are able to compute the shape of the known pulse after propagation through an absorptive and dispersive medium purely by measurement of the optical depth.

2.3 Experimental Setup

As indicated by the Kramers-Kronig relation, a bulk material with a sharp absorption band will have a corresponding sharp change in the real part of the index of refraction. The availability of femtosecond Ti:Sapphire lasers with pulse lengths of tens of femtoseconds and center wavelengths of 800 nm suggests that precursors are more likely to be observable in this context in materials with sharp absorption bands at or near 800 nm. For this experiment we select the proprietary dye NP800 (Exciton) which is extremely soluble in the organic liquid 1,1,2,2-tetrachloroethane. We dissolve the NP800 in the 1,1,2,2-tetrachloroethane for a final dye concentration of 10 g/l. A droplet of this solution is placed between two microscope cover slips which each have a thickness of about 190 μm. The solution is held in place between the glass slips by surface tension, and the unit is placed on a support which holds the slips in the path of the beam.

While a reference absorption spectrum of the organic dye is available from the originating company, we independently characterize the optical depth of the dye solution between the cover slips as a function of wavelength. By shining a broadband incandescent light through the solution and through the cover slips with dye, we obtain an experimental measurement of $\tau(\omega)$. This yields the absorption spectrum over the bandwith of our spectrometer, and we assume that the absorption is equal to zero elsewhere when computing the total refraction using the Kramers-kronig relations. As noted in section 2.2, this only affects the uninteresting overall pulse delay while leaving the shape of the pulse including precursors unaffected. The

calculated total refraction is plotted in figure 2.1. The total refraction is plotted over a large range for mathematical clarity, but only the values of $N(\omega)$ within the bandwidth of the laser are relevant to the actual propagation of the pulse. The

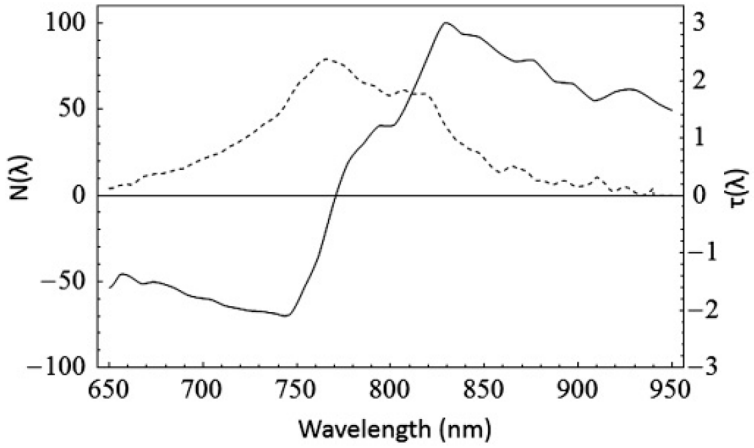

Figure 2.1: Measured absorption curve (dashed) and calculated total refraction (solid) of NP800 in 1,1,2,2-tetrachloroethane

laser pulses are then directed through the dye solution, shown schematically in figure 2.2. The pulses are generated by a femtosecond laser (Rainbow, Femtolasers) with a center wavelength of 800 nm and a FWHM pulse duration of about 9 fs. The pulse energy is approximately 2 nJ with a repetition rate of about 80 MHz. The pulse is unfocused and the relatively low pulse energy ensures that the propagation occurs entirely in the linear regime. The pulse shape is measured by interferometric autocorrelation before and after propagation through the dye layer.

2.4 Genetic Algorithm and Pulse Characterization

We characterize the laser pulse by means of an interferometric autocorrelator. Such an autocorrelator characterizes pulses by splitting the pulse with a beamsplitter,

Figure 2.2: Schematic diagram of the experiment

delaying one of the resulting pulses by a variable translation stage, and recombining the pulses through a second-order nonlinear crystal which responds to the square of the instantaneous intensity. The total energy of the frequency-doubled light for each translation stage delay is recorded and results in an autocorrelation trace given by

$$I(\tau) \propto \int_{\infty}^{\infty} |\left(E(t) + E(t-\tau)\right)^2|^2 \, dt \tag{2.6}$$

Unfortunately there is no analytic method to cleanly solve for $E(t)$ given $I(\tau)$. In fact the interferometric autocorrelation is symmetric with respect to replacement of t with $-t$ so at any rate the directon of time of the pulse is not available by autocorrelation alone. However, in principle the interferometric autocorrelation uniquely determines the pulse up to the direction of time ambiguity, though Trebino [48] notes that in some cases near-ambiguities are possible.

We attempt to conduct the most accurate retrieval of the pulse from the autocorrelation by using a genetic algorithm which reconstructs the pulse via a low-order polynomial in the phase combined with a pointwise phase function over the bandwidth of the pulse. The pulse retrieval method operates in the following way: we begin with the measured intensity spectrum (figure 2.3) as observed by a spectrometer. The initial assumption is that the pulse is transform limited with a zero phase

throughout its spectral bandwidth:

$$E(t) = \mathrm{Re}\left[\frac{1}{\sqrt{2\pi}}\int_{-\infty}^{\infty} A(\omega)e^{i\omega t}\,d\omega\right]. \tag{2.7}$$

This yields an the autocorrelation for the initial guess (figure 2.4). We vary the phase of the complex amplitude $A(\omega)$ by means of the genetic algorithm and calculate the resulting autocorrelation from equation 2.6. The integral of the square of the difference between the calculated and measured autocorrelation is then computed. The genetic algorithm then iteratively adjusts the phase function of the pulse in order to minimize the difference between the observed and calculated autocorrelations.

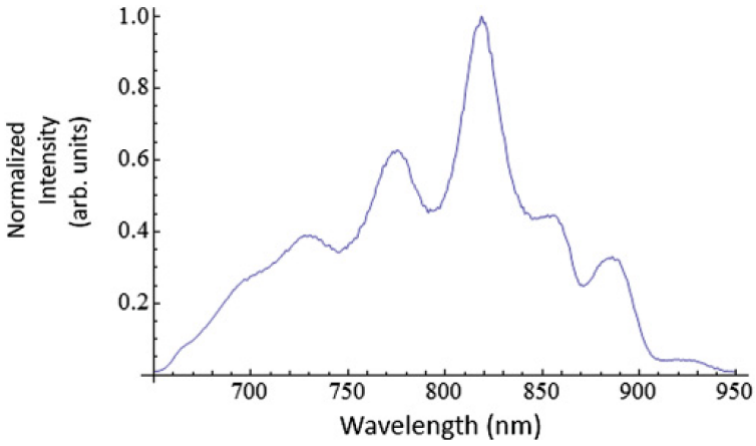

Figure 2.3: Measured intensity spectrum before the dye cell

Once the genetic algorithm calculates a phase function which results in a minimum integrated least squares difference between the calculated and observed autocorrelations, the algorithm outputs the complex phase (figure 2.5) which generates an autocorrelation which most closely matches the observed autocorrelation (figure

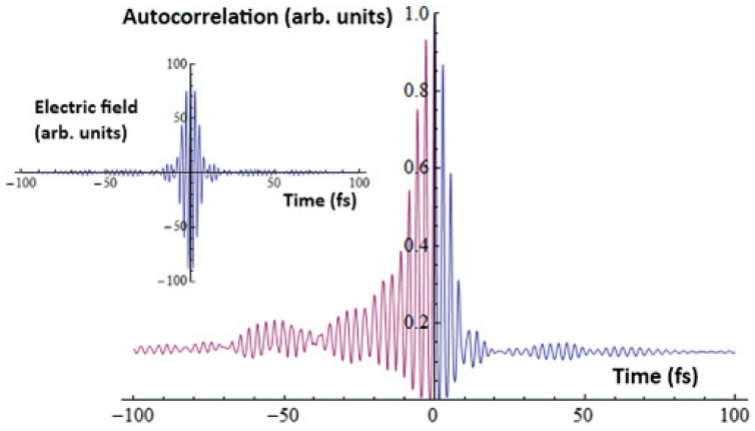

Figure 2.4: Initial electric field guess (inset) with calculated autocorrelation from initial guess (right half of graph) and measured autocorrelation (left half of graph)

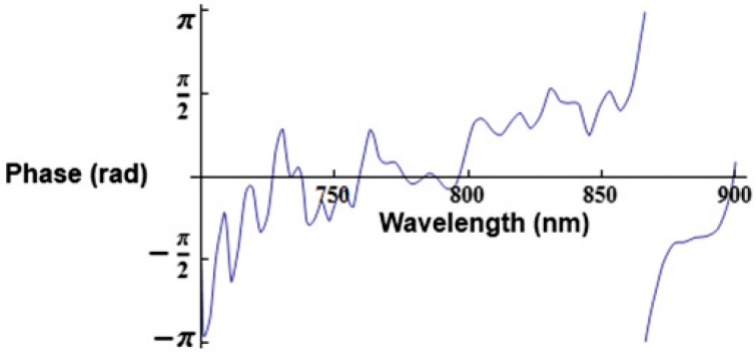

Figure 2.5: Spectral phase retrieved from genetic algorithm

2.6). To resolve the direction of time ambiguity we also insert the two cover slips (without the dye) before the autocorrelator and used the known dispersive characteristics of the BK7 glass to compared the autocorrelation expected from the glass with the autocorrelation actually observed. As a secondary check we insert the cover slips with dye into one of the arms of the autocorrelator, resulting in the measurement of a cross-correlation. This is a less robust method of resolving the direction of time

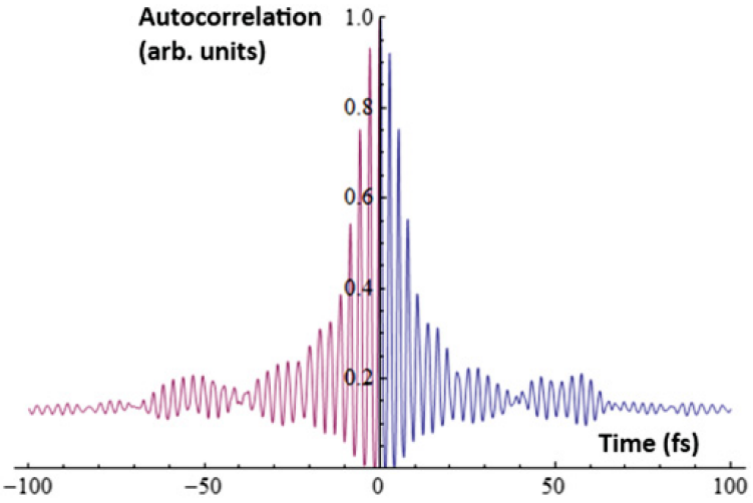

Figure 2.6: Calculated autocorrelation from genetically retrieved pulse (right half of graph) and measured autocorrelation (left half of graph)

ambiguity because both the shape of the original pulse and the shape of the propagated pulse are potential sources of error. Nonetheless, it is useful in confirming the direction of time as observed by the autocorrelation measurements.

The pulse as retrieved by the autocorrelator and genetic algorithm (shown in figure 2.7) contains significant noise away from the peak. This is an unavoidable consequence of the sensitivity of the inverse Fourier transform to small errors in the retrieved pulse. As a consequence we analyze those pulse features which are large in amplitude and located near the pulse maximum. the fourth-power dependence of the interferometric autocorrelation on the field strength ensures that these high-amplitude features are the dominant contributors to the autocorrelation, and are consequently less susceptible to noise in the pulse retrieval algorithm. Small features far from the pulse peak should not be assumed to correspond very precisely to the actual laser pulse [95].

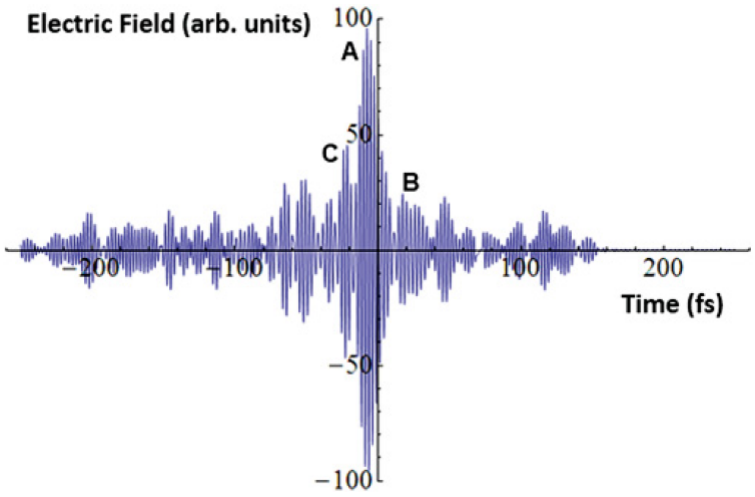

Figure 2.7: Initial electric field retrieved by the genetic algorithm, along with labeled reference peaks

2.5 Pulse Propagation Simulation

With the knowledge of the initial shape of the pulse and the dispersive and absorptive characteristics of the dye and glass, we can calculate the shape of the pulse after propagation. As discussed in sections 2.1 and 2.2, optical precursors can be characterized in terms of their relative velocity to other portions of the pulse and their attenuation behavior with regard to the distance of propagation. In attenuation the precursor does not necessarily attenuate exponentially with distance, though the pulse as a whole does obey the frequency-domain BLB law. a specific temporal subfeature of the pulse, such as a precursor, may leach energy from another region of the pulse, maintaining its amplitude at the expense of adjacent parts of the pulse. This should not be taken as a violation of the BLB law, as each spectral component is separately attenuated with distance in the usual linear way.

Because precursors are closely associated with sharp near-discontinuous features of a pulse, characterization of the attenuation with distance of these features can be

indicative of precursors or precursorlike pulse behavior. We therefore select features appearing in the genetically determined pulse which most closely fit this description and simulate their evolution as a function of distance propagated in the dye. The initial pulse shape determined by the genetic algorithm and shown in figure 2.7 contains sharp internal features with rise times on the order of one optical cycle of approximately 2.7 fs. The fourth-power dependence of the autocorrelation signal on the field strength leads us to consider the dynamics of the temporally shape central pulse features of the highest amplitude, also labeled in figure 2.7.

We simulate the propagation of this pulse using the pulse propagation equation, which we evaluate numerically. Using the definition of the optical depth $\tau(\omega) = \alpha(\omega)d$ and dropping the unknown overall phase $e^{i\frac{\omega}{c}x}$, which is not necessary for computing the autocorrelation, we have the propagated pulse

$$E(t) = \frac{1}{\sqrt{2\pi}} \int_0^\infty A(\omega) e^{i\phi\left(\frac{\omega}{c}N(\omega)+\tau(\omega)/2\right)} e^{2n_g(\omega)x}\, d\omega + \text{c.c.}. \tag{2.8}$$

Here $n_g(\omega)$ is the real refractive index of the BK7 glass cover slip, and x_g is the 190 micron thickness of one cover slip. We do not include the very small reflection coefficients at the glass-dye interfaces, as the coefficients cannot be precisely calculated without knowledge of the thickness of the dye layer. However, the close match between the refractive indices of the BK7 glass ($n \approx 1.51$) and tetrachloroethane ($n \approx 1.49$) allows a Fresnel equation estimate of the reflection coefficient, yielding a reflectivity of less than 0.1%. The additional effect of the dye dispersion of reflection can be estimated by setting a typical dye layer thickness of 2 microns in equation 2.3, which yields a negligible frequency-dependent chance in the already small reflection coefficient. The intensity of multiply reflected pulses transmitted from within the dye layer is proportional to the square of the reflection coefficient and can be

neglected as well. After calculating the electric field of the propagated pulse at the experimentally accessible value of $\phi = 1$, we can compare the observed autocorrelation to the autocorrelation calculated from the simulated pulse. The calculated pulse after passing through the dye is presented in figure 2.8, while the observed autocorrelation and the calcualted autocorrelation of the pulse after the dye are presented in figure 2.9. Good agreement can be seen around the central portion of the auto-

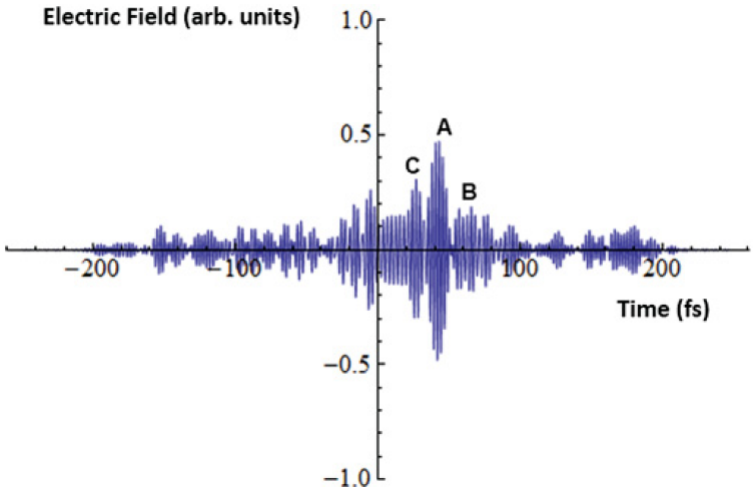

Figure 2.8: Calculated pulse after passing through due solution, with labeled reference peaks

correlation, indicating the close association between theory and experiment for the high-amplitude features in the calculated pulse. The theoretical autocorrelation is less accurate in the wings of the signal. This likely indicates that the genetically retrieved pulse may not well represent the smaller outer features of the pulse. We then calculate the pulse shape for dye propagation distances between zero and the total dye thickness $\phi = 1$. We track the labled features and measure their attenuation as the propagation distance is varied (figure 2.10).

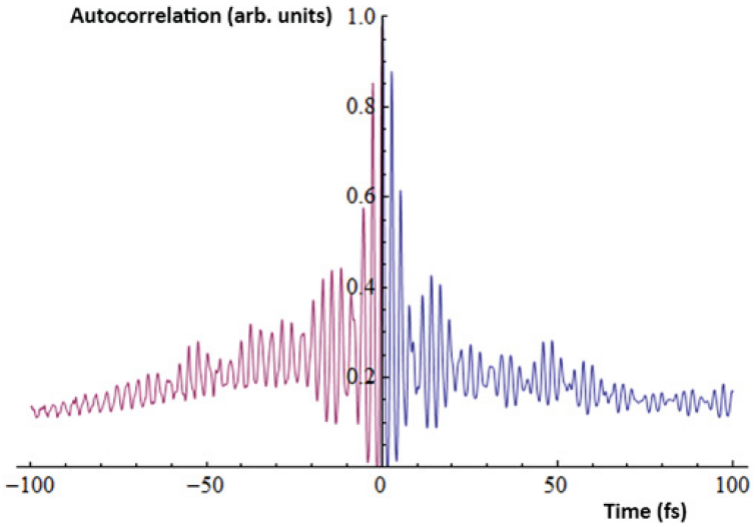

Figure 2.9: Calculated pulse after passing through due solution, with labeled reference peaks

The pulse peak (Feature A) decays exponentially with a best-fit dimensionless attenuation rate of 0.528 while the secondary Feature B decays with a much longer best-fit attenuation rate of 0.187 and the secondary Feature C decays with an intermediate attenuation rate of 0.297. This variation of attenuation length for each feature is a signature of precursorlike behavior.

2.6 Summary

We observe a signature for enhanced attenuation distance characteristic of optical precursors by means of interferometric autocorrelation and genetic algorithm phase retrieval supplemented by numerical simulation. Limitations in the accuracy of the autocorrelation method prevent full knowledge of the precursor fields. However, the behavior of the high-amplitude portion of the propagating field is readily discernible. Those features of the high-amplitude portion which correspond to few-cycle rise times exhibit reduced exponential attenuation with respect to distance. This behavior is

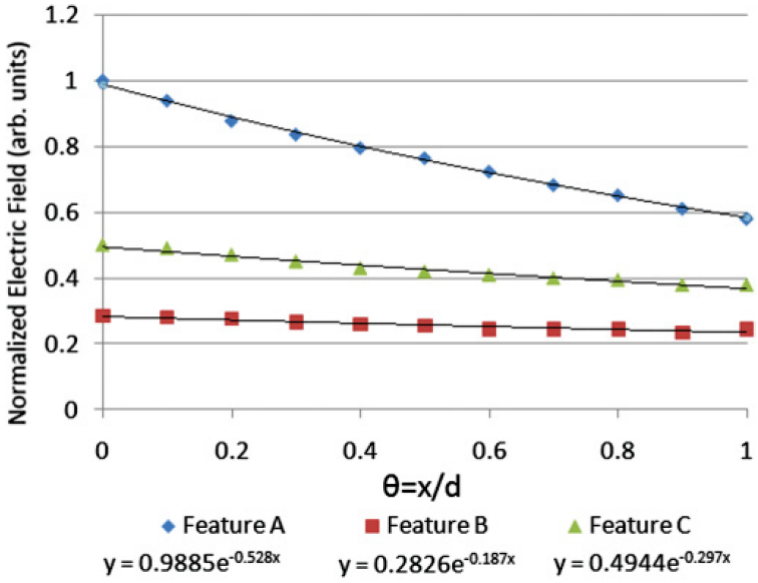

Figure 2.10: Distance attenuation of selected time-domain pulse features with exponential best-fit curves

consistent with current theoretical knowledge of precursor behavior.

3. ONSET OF FILAMENTATION UNDER EXTERNAL FOCUSING AND OPTICAL BREAKDOWN

3.1 Introduction

The propagation of laser beams of low intensity in linear dielectrics is a generally well-understood phenomenon within the laws of classical optics. As the intensity increases, nonlinearities such as the optical Kerr effect and the generation of plasma through ionization serve to modulate the effective complex refractive index of a medium, leading to phenomena such as self-focusing, beam breakup, and femtosecond laser filamentation [46, 47]. These regimes of high intensity beam propagation are more difficult to model computationally in view of the $3+1$ dimensional nature of the problem as well as large uncertainty associated with higher-order nonlinear coefficients in physical dielectric media of interest [16]. The high intensity is also a barrier to accurate experimental pulse measurement of pulses undergoing filamentation or optical breakdown due to the fact that measuring devices generally cannot tolerate pulses of very high intensity, and correspondingly optical damage is one of the methods for experimentally characterizing filaments [18, 19, 53].

One possibility for avoiding the difficulty associated with exposing a measuring device to extremely intense pulses is to scatter a low-intensity unfocused pulse of light off the nonlinearities induced in the dielectric by the propagation of the intense pulse. Controlling the delay of the probe with respect to the pump allows time-resolved measurements of pulse propagation, allowing direct shadow imaging [80], holographic techniques [82, 83, 88, 90, 96], shadowgraphs [84–86] or imaging based on the rotation of the polarization of the probe pulse [77, 79, 92]. We extend this technique to produce direct time-resolved microscope-style images of the nonlinear

propagation of ultrashort pulses through air under external focusing.

One of the longstanding issues in filamentation physics is the definition of filamentation as distinguished from optical breakdown, and the characterization of the regime intermediate between the two. Filamentation is variously defined in terms of intensity clamping [13], supercontinuum generation and conical emission [62], or in terms of the filament geometry by virtue of maintaining a small beam waist over a distance longer than the classical Rayleigh length [97]. For some pulse propagation regimes such as terawatt beams propagated over kilometers, these conditions are all clearly satisfied [26, 59]. In the intermediate cases of stronger external focusing, the definitions disagree somewhat and the question of whether or not a given propagation regime can be called "filamentation" is less clear, leading to experimental work on the behavior of filaments and filament-like structures under external focusing [60, 62, 66, 67, 91]. In this paper, we experimentally analyze situations of optical breakdown under external focusing in an effort to resolve some of these questions.

In the technique reported here, we generate optical breakdown by means of an intense externally-focused femtosecond pulse in air. We use a weak unfocused femtosecond pulse as a "camera flash" to illuminate the region of breakdown in a time-resolved manner. This probe pulse is directed into a microscope configuration and imaged onto a CCD, allowing us to directly view the pulse as it propagates on femtosecond time scales.

3.2 Conceptual Framework

In linear pulse propagation, the optical properties of a dielectric propagation medium are determined by its complex refractive index, which determines the phase velocity and absorption of the light. For intense light, the polarization of the medium is a power series in the applied fields, leading to an effective intensity-dependent index

of refraction [9] given to first order in intensity by

$$n = n_0 + n_2 I,$$

where n_0 is the linear index of refraction and n_2 is the leading order term in the nonlinear index of refraction. In air, $n_2 = 5.38 \times 10^{-19}\,\mathrm{cm}^2/\mathrm{W}$ [98]. A pulse with a Gaussian spatial profile therefore experiences an index of refraction which is greatest towards the center of the pulse, leading to a lensing effect, self-focusing, and eventual collapse of the pulse for instantaneous peak powers greater than the critical power

$$P_{\mathrm{crit}} = \frac{\lambda^2}{8\pi n_0 n_2},$$

which takes typical values of approximately 300 MW in air and 300 kW in fused silica [23]. In the simplest model, collapse of the beam due to self-focusing is arrested when the intensity becomes high enough to generate plasma with a negative contribution to the index of refraction [46]. This occurs at intensities of approximately $I = 7{\times}10^{13}\,\mathrm{W/cm}^2$, leading to refractive index changes of approximately $n_2 I = 3.5{\times}10^{-5}$.

Aside from self-action effects on the high-intensity pulse, the refractive index changes generated by the Kerr effect and the creation of plasma affect light which is propagating through the affected region from any direction. The refractive index is a measure of phase shift per wavelength propagation distance,

$$\delta\phi = n\frac{x}{\lambda},$$

where x is the propagation length and λ is the wavelength of the light. For femtosecond laser filaments of notional diameter 100 microns with $\lambda = 800\,\mathrm{nm}$, the phase shift in air for a probe beam passing perpendicularly through the filament

will be on the order of 0.1 - 1%. This suggests the possibly of directly imaging the scattered light. For pulses of light which are more tightly focused than a purely self-trapping but otherwise unfocused beam, including pulses tightly focused enough to begin optical breakdown, the refractive index change will be larger and the phase shifts correspondingly easier to image. Other index changes such as the dispersion and absorption due to plasma generated through multiphoton ionization may also be imaged.

The nonlinearities induced by the intense pulse occur over various time scales, from femtoseconds in the case of the optical Kerr effect to nanoseconds for the plasma generated to recombine. Imaging these nonlinearities with a low-intensity femtosecond probe pulse allows separate measurements of these phenomena by the choice of direct imaging or birefringence imaging, along with time-resolution by varying the delay time between the two pulses.

3.3 Experimental Configuration

Our experimental apparatus (shown in figure 3.1) consists of an amplified femtosecond laser (Coherent Legend Elite, 800 nm center wavelength, 50 fs, 4 mJ maximum pulse energy) which can produce ultrashort pulses at a rate of 1 kHz or single pulses on command. The pulses are separated by a glass wedge which transmits approximately 90% of the incoming pulse and reflects approximately 5% of the incoming pulse. The reflected portion of the pulse is passed down an adjustable delay line and used as the low-intensity imaging probe. The transmitted portion of the pulse is passed through a lens which focuses the main pulse into a filament or near-filament configuration. The focusing lens is mounted on a vertical translation stage in order to move different parts of the filament or optical breakdown into view of the imaging lens and CCD.

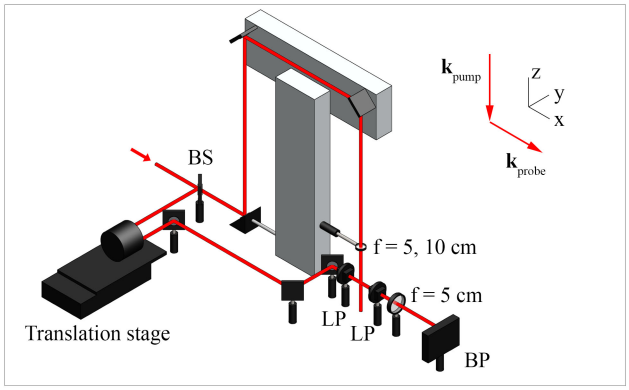

Figure 3.1: Experimental apparatus for optical breakdown imaging experiment

The unfocused probe beam is directed to intersect the focus of the main beam along the perpendicular direction. We produce an image by directing the imaging beam through a 5 cm focal length lens which is between the filament and the CCD (Spiricon SP620U). By varying the distances between the filament and imaging lens, and the imaging lens and the CCD, we may vary the magnification of the image of the filament. The CCD is an array of 1600 by 1200 pixels, with a pixel separation of 4.4 μm. With known magnification from the object plane to the image plane, dimensions of observed structures in the image plane can be used for mensuration of features in the object plane. In this present work the distance from the point of optical breakdown to the imaging lens is 6.5 cm, and the distance from the imaging lens to the CCD plane is 28 cm. This yields a magnification of approximately 4.3 at the image plane. The imaging lens has a radius of 1.75 mm, yielding a numerical aperture of about 0.27 for a theoretical resolution of about 3.0 microns. We verified that the resolution is at least better than 10 microns by imaging optical fibers of known size, and in this experiment we are interested in nonlinearities which are of at least 50 microns in spatial extent.

The translation stage (Newport GTS150) controlling the delay of the imaging

pulse is capable of stepping in 50 nm increments, which corresponds to a change in the light travel time of less than one femtosecond. The temporal resolution of the 'movie' produced by the succession of images at varying delay is thus limited by the temporal length of the probe pulse, of about 50 fs. This is adequate to observe the femtosecond-scale nonlinearity of the Kerr effect, and much better than necessary to examine pico- and nanosecond scale nonlinearities involving ionization and recombination.

Once the timing between the high-intensity pulse and the low-intensity pulse is set by the translation stage, we can observe the propagation of the pulse in a "co-moving" frame by translating the lens which focuses the high-intensity pulse along its direction of propagation. The high-intensity pulse and the imaging pulse will meet at the same spatial position in the lab frame, but the position of this intersection with respect to the focus of the high-intensity pulse can be independently set. Thus the image of the pulse will appear at the same location on the CCD while still allowing the entire propagation to be imaged in a time-resolved manner.

For direct imaging of the region of optical breakdown, the area of optical breakdown is illuminated by the probe beam and imaged by the lens directly onto the CCD. For imaging of induced birefringence, a polarizer rotated at 45 degrees with respect to the probe beam is placed directly in front of the CCD while an orthogonally-oriented polarizer is placed behind the region of filamentation as shown in figure 3.1. In the birefringence-imaging configuration no light reaches the CCD except for the portion of the probe light which has been rotated by induced birefringence from the high-intensity pulse, along with the plasma fluorescence which gives a constant unpolarized background.

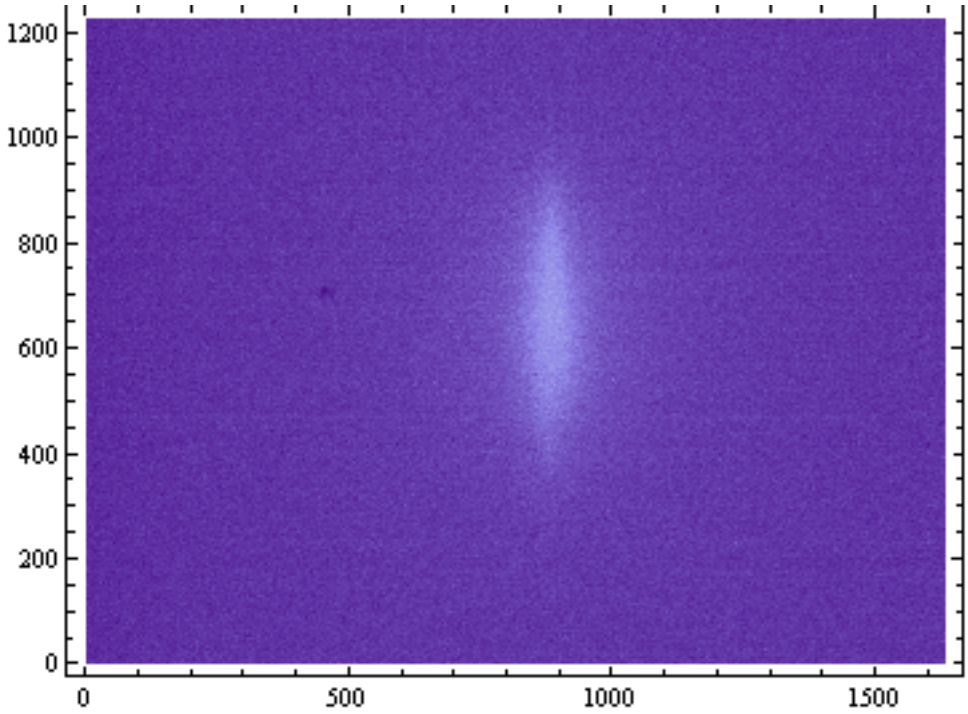

Figure 3.2: Image of the fluorescence produced by the plasma generated by the 5 cm lens. Scale is in microns.

3.4 Experimental Results

This experiment analyzed the time-resolved propagation of femtosecond pulses focused by 5 cm and 10 cm focal length lenses. For both cases, the pulse energy is measured to be 1.68 nJ and the pulse length is approximately 50 fs as measured by autocorrelator. By blocking the time-resolved imaging pulse, we directly imaged the region of visible breakdown and corresponding plasma fluorescence. For the 5 cm lens, the region of detectable fluorescence is approximately 750 microns along the direction of propagation and 100 microns in diameter at the focus, as shown in figure 3.2. For the 10 cm lens, the region of detectable fluorescence is approximately 900 microns along the direction of propagation and 80 microns in diameter at the focus, as shown in figure 3.3.

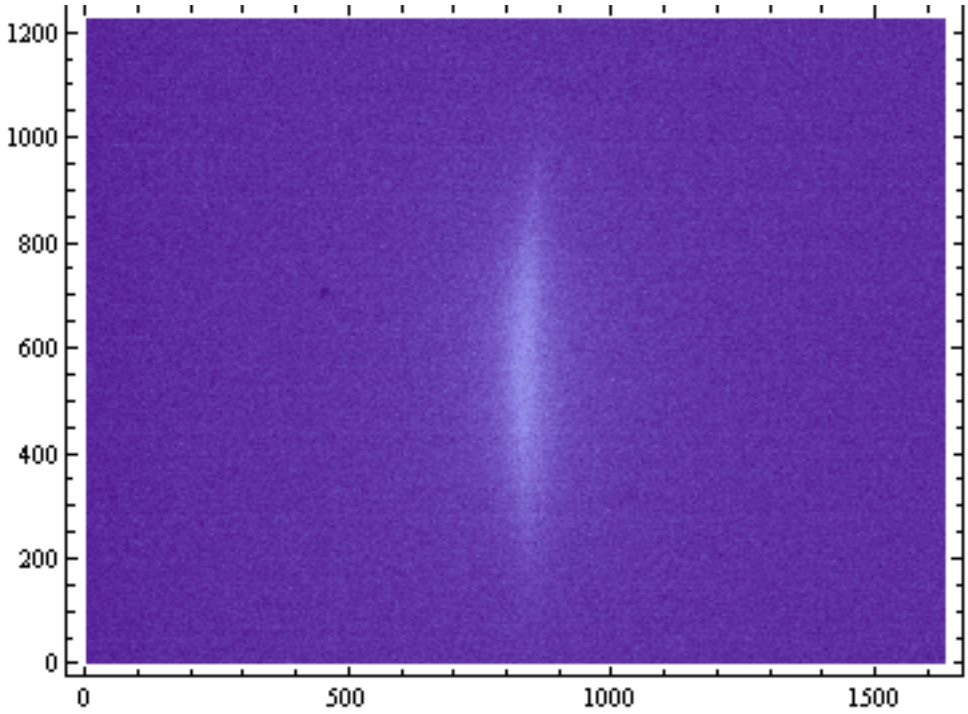

Figure 3.3: Image of the fluorescence produced by the plasma generated by the 10 cm lens. Scale is in microns.

We then allow the probe pulse to refract off the region of optical breakdown and image the result over a range of time delays between the pump and probe pulses. A time-resolved image of the breakdown region produced by the 5 cm lens at a time delay where the pulse is near the center of the breakdown region in shown in figures 3.4 and 3.5. At the leading edge of the pulse (which travels from top to bottom in these images), the pulse itself is visible as a roughly spherical object at the head of a trailing tail of generated plasma which we observe to persist essentially unchanged in shape and visibility over the several hundred picoseconds worth of time-delay range afforded to us by the translation stage.

We can distinguish between the plasma and Kerr nonlinearities by positioning crossed polarizers on either side of the region of breakdown. This generated plasma

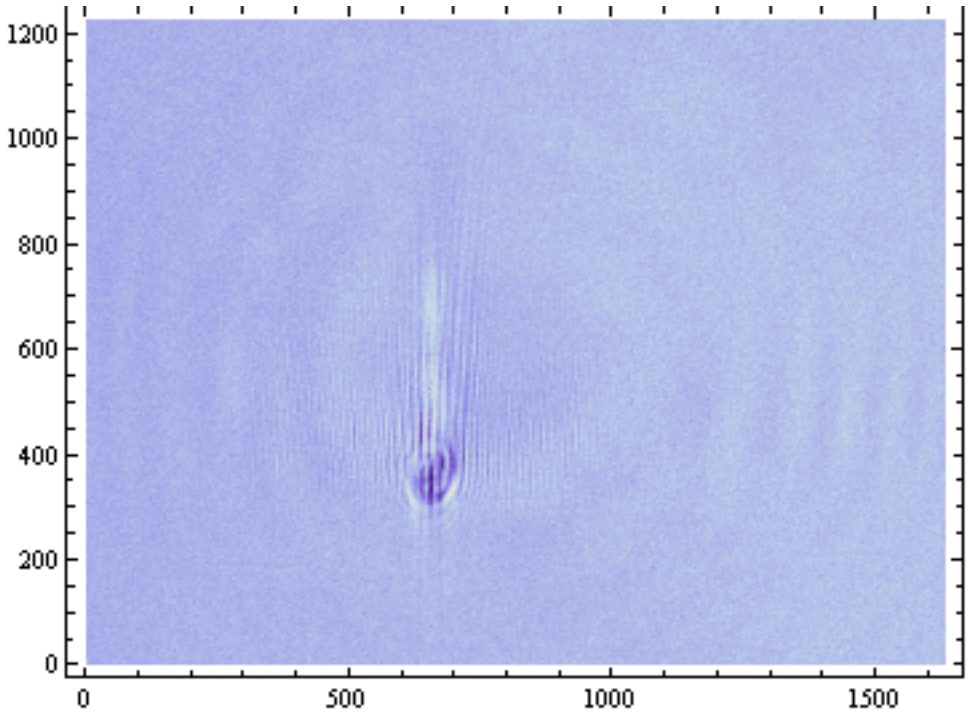

Figure 3.4: Time-resolved image of the plasma generated by the 5 cm lens, as the pulse approaches the midpoint of the region of optical breakdown. Scale is in microns.

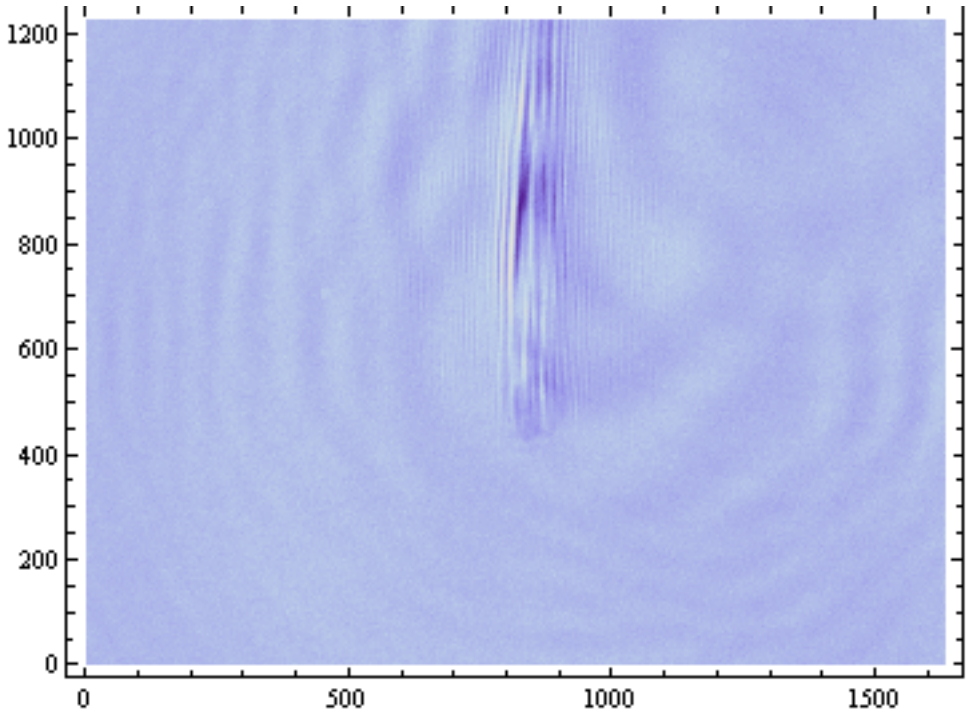

Figure 3.5: Time-resolved image of the plasma generated by the 10 cm lens, after the pulse has left the region of breakdown toward the end of its observable propagation. Scale is in microns.

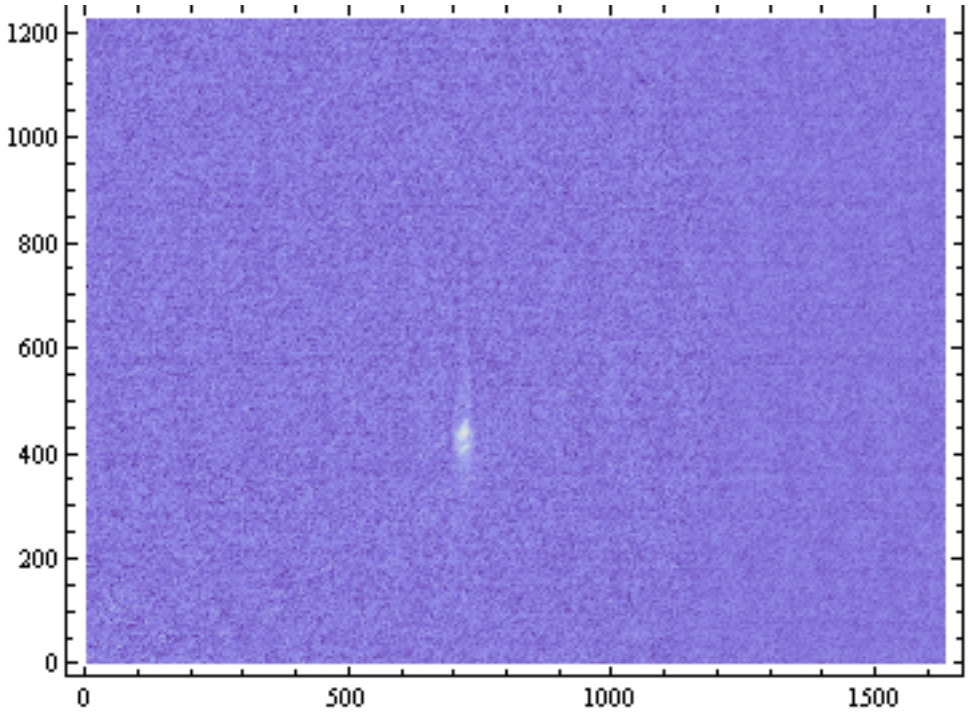

Figure 3.6: Time-resolved image of the birefringence generated by the 5 cm lens. Scale is in microns.

is isotropic and thus not birefringent, while the Kerr effect depends on the orientation of the electric field and results in induced birefringence. The birefringence (figure 3.6) is small and the light for which polarization is rotated is thus small, however, it is consistently visible and very similar in size to the semi-spherical area which is easily visible in the ordinary direct images.

This process of imaging the plasma fluorescence without the probe, imaging the breakdown region directly through the time-resolved probe pulse, and imaging birefringence through the time-resolved probe pulse is then repeated with the breakdown generated by the 10 cm focal length lens.

The femtosecond laser pulse emitted by the amplifier in our experiment has an initial radius measured by knife-edge to be $w_{\mathrm{i}} = 0.46\,\mathrm{cm}$. Upon focusing through a

lens of focal length f, the geometrically expected focal spot size for a Gaussian beam is

$$w_0 = \frac{\lambda}{\pi(w_\mathrm{i}/f)}.$$

For 5 and 10 cm lenses, this gives a w_0 of 2.78 and 5.54 microns respectively. The Rayleigh length is given by

$$z_r = \frac{\pi w_0^2}{\lambda},$$

leading to values of 30 and 120 microns respectively.

In both cases the experimental observations show an actual beam waist which is much larger than the classical beam waist: about 102 ± 5 microns in the case of focusing with the 5 cm lens and 105 ± 5 microns in the case of the 10 cm lens. Assuming that the entire energy of the pulse is distributed approximately uniformly within the observed radius of plasma generation, this corresponds to a clamped intensity of $3.9 \times 10^{14}\,\mathrm{W/cm^2}$, in reasonable agreement with the $2.5 - 5.0 \times 10^{14}\,\mathrm{W/cm^2}$ value measured by Liu [91] and other workers [99]. This radius and intensity is not observed to be strongly dependent on the external focusing conditions, indicating that the usual intensity clamping is accompanied by "size clamping" of the transverse radius of the pulse.

The pulse is visible under imaging over a distance of 1440 ± 100 microns and 1790 ± 100 microns for the 5 and 10 cm focal length lenses, respectively. This is one to two orders of magnitude longer than the 30 and 120 micron classical Rayleigh lengths, and approximately double the length of the visibly observable region of plasma fluorescence. Over this propagation length, the diameter of the pulse is not observed to change by more than approximately 10 percent.

Within the region of plasma generation, the plasma is observed to be generated in a filamentary structure which persists at least over the nanosecond-scale delay achiev-

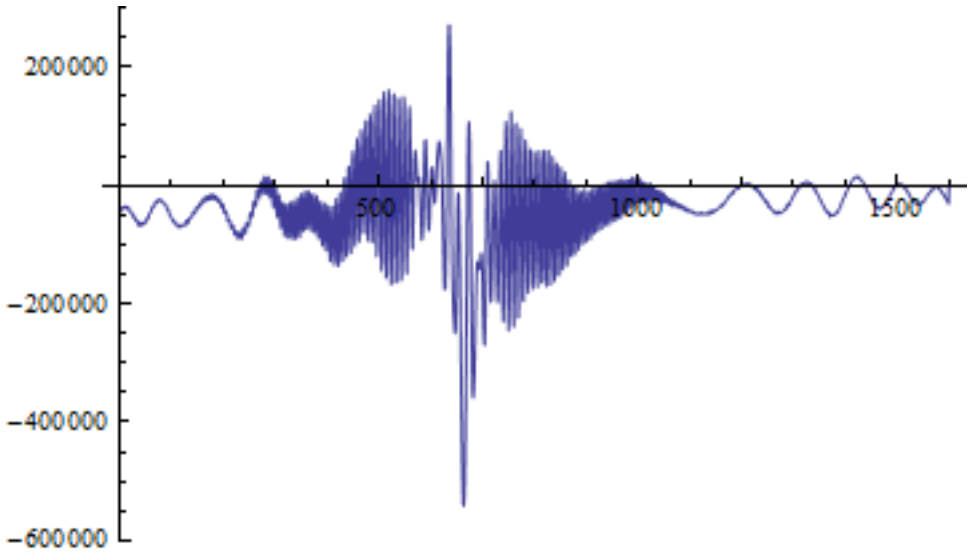

Figure 3.7: Intensity profile of a slice through the image of the generated plasma. Scale is in microns on the x-axis, arbitrary intensity units on the y-axis.

able by the translation stage in this experiment. Horizontally slicing the plasma trail in figure 3.4 and plotting the result in figure 3.7 provides a means for measuring the scales of the structure of the generated plasma. The Fourier transform of this slice is shown in figure 3.8.

The Fourier transform in figure 3.8 has peaks at approximately 70 and 110 inverse millimeters. These corresponds to features of typical size 14.3 and 8.3 microns respectively. The 14.3 micron features correspond to the size of the generated filamentary plasma structures, while the 8.3 micron features correspond to the smaller diffraction fringes which are generated by the plasma column as a whole. The peak pulse power in this experiment is on the order of the critical power for self-focusing in air, so beam breakup is not expected. However, the strong nonlinearity will result in strong coupling between spatial modes as described in section 1.2.7. As the pulse as a whole is clamped in intensity, small variations within the clamped region may couple to each other, form relatively small variations in intensity, and generate

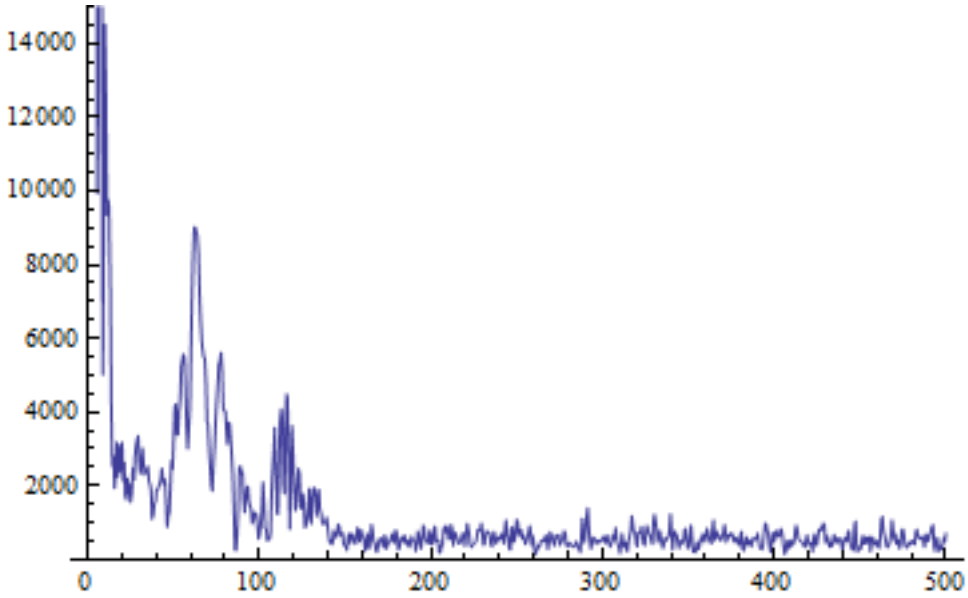

Figure 3.8: Fourier transform of the slice through. Scale is in inverse millimeters on the x-axis, arbitrary units on the y-axis.

substantially space-varying densities of plasma due to the strong approximately I^8 nonlinearity governing multiphoton ionization in air.

3.5 Discussion

Chin [23] notes that strong external focusing leads to stronger plasma generation than filamentation from a loosely-focused beam; the stronger focusing results in much stronger plasma generation through multiphoton ionization, leading to intensity clamping. Our estimate of the clamped intensity within the pulse during optical breakdown is about an order of magnitude larger than the typical value of $10^{13}\,\mathrm{W/cm^2}$ [16, 46] observed in loosely-focused femtosecond filaments. This is possibly due to the greater intensity required for the increased plasma generation which compensates for the combined effects of geometric focusing and self-focusing. Small differences in intensity lead to large differences in ionization through the $\sim I^8$ nonlinearity of plasma generation in air [13], which also likely accounts for the fact that the

observed filamentary structure is considerably longer in spatial extent than the observed plasma glow. Because "size clamping" is enforced by the focusing vs. plasma defocusing balance at intensities which are clamped within a certain range but not precisely fixed, this small range of intensities can produce large swings in plasma density and observed plasma fluorescence. While the process of optical filamentation is often defined in terms of intensity clamping, filamentation is also frequently contrasted with the optical breakdown which occurs in conditions of strong external focusing such as occur in this experiment.

The results of this present work indicate that some forms optical breakdown can reasonably be included in a definition of filamentation which is based on either intensity clamping or maintaining a small transverse size beyond the Rayleigh length. Conversely, if a definition of filamentation is adopted which excludes optical breakdown as a matter of course, it must be recognized that optical breakdown, like filamentation, is nonetheless a regime of pulse propagation where classical optics ceases to be a good description of the propagation geometry. In this regime, parameters such as the classical beam waist and Rayleigh range are no longer valid and filament-like plasma distributions and cross-sectional fluences can be expected.

4. BEAM BREAKUP AND MULTIPLE FILAMENTATION IN LIQUID WATER

4.1 Introduction

Femtosecond laser filaments result from a dynamic balance between nonlinear self-focusing, diffraction, and plasma defocusing. The coefficients for self-focusing as a function of intensity vary greatly between various materials (see table 1.1), most notably as a function of density. In air the critical power P_{cr} for self focusing is about three orders of magnitude larger than the critical power for self-focusing in typical condensed matter dielectrics such as water and glass. Below the critical power, the spreading of the beam due to diffraction is greater in magnitude than the self-focusing induced by the intensity-dependent refractive index induced by the optical Kerr effect. In these cases the propagation of the beam or pulse is governed by classical linear optics. Essentially all non-laser light and most CW laser radiation falls into this regime. Just about the critical power, the Kerr effect self-focusing is strong enough to overcome the spread of the beam due to diffraction and the beam begins to focused. This focusing increases the intensity which further enhances the self-focusing and the beam collapses. The collapse is eventually arrested by higher-order nonlinearities, in particular the formation of plasma which has a negative contribution to the index of refraction. The beam size and intensity at which these effects are in dynamic balance comprises an optical filament. The critical power itself is given by [1]

$$P_{cr} = \frac{\pi(0.61)^2\lambda_0^2}{8n_0n_2}. \tag{4.1}$$

In water the critical power is $P_{cr} = 1.17\,\mathrm{MW}$.

For pulses with an instantaneous power much greater than the critical power, instabilities in the balance between self-focusing and plasma-defocusing lead to beam breakup (For theoretical background see section 1.2.5. For an overview of the literature, see the reviews in [13, 16, 23, 100], as well as additional references in section 1.3.2). In general, a pulse with an instantaneous power P which is greater than the critical power by some factor $P = NP_{cr}$ will break up into approximately N distinct filaments each containing a power of about P_{cr} and sharing a common energy reservoir. Because the critical power in air is on the order of 10 GW, it is difficult to explore the dynamics of beam breakup in air with tabletop lasers. In the present work, we use an amplified Ti:Sapphire laser (Coherent, Legend elite) of available nominal pulse energy 2 mJ and pulse FWHM duration 35 fs. In principle this laser delivers a peak power on the order of 50 GW. With external focusing this is sufficient for one or perhaps two filaments in air, this is badly inadequate for exploring the regime of pulse powers which are many times the critical power. In condensed matter the critical power is lower by about 3 orders of magnitude, and the peak power of the amplified Ti:Sapphire laser is thus several orders of magnitude more than the critical power in most solid-state media. Condensed matter in the solid state is susceptible to permanent damage tracks, which makes it a poor test medium for time-resolved filament measurements which require the propagation of many identical pulses through identical conditions. The damage tracks can provide some information about the filament which created it, but not in a time-resolved manner [17, 19, 52]. Liquid is inherently self-healing in this context, which makes it ideal at examining filaments in condensed manner on a time-resolved shot-by-shot basis.

This experiment uses a time-resolved imaging technique to resolve the behavior of a femtosecond pulse incident on liquid water both spatially and temporally. We are

primarily interested in a characterization of the breakup of the beam as it transitions from its original configuration as a mostly-Gaussian laser pulse, through the initial development of instability in the transverse intensity profile, before finally transitioning into a mature filament bundle where each filament possesses approximately the critical power for self-focusing.

4.2 Conceptual Framework

The critical power for self-focusing is calculated based purely on the instantaneous power of the laser pulse such that a balance is achieved between self-focusing and diffraction spreading. The intensity of the light (and thus the degree of self-focusing) over the face of the beam scales inversely as the square of the radius of the beam, but the angle of diffractive spreading also scales inversely with the square of the beam radius at the waist. As such, the balance between the two effects is maintained in principle for any Gaussian beam at the critical power, regardless of its cross-sectional size and thus its intensity. However, once a beam achieves the critical power or greater, it will begin the process of self-focusing in excess of diffractive spreading leading to eventual collapse and optical breakdown or filamentation. The propagation length scale over which the beam collapses from its initial radius to a filament is dependent on the initial beam radius [13]. Marburger [44] gives a formula for the collapse distance

$$z_f = \frac{0.367ka_0^2}{\left\{\left[(P/P_{cr})^{1/2} - 0.852\right]^2 - 0.0219\right\}^{1/2}}. \tag{4.2}$$

When the beam undergoes external focusing through a positive lens of focal length f before encountering the nonlinear medium, the collapse distance is reduced to

$$z'_f = \frac{z_f f}{z_f + f}. \tag{4.3}$$

For the parameters of our beam ($a_0 = 0.46\,\mathrm{cm}$, $\lambda = 800\,\mathrm{nm}$), the self-focusing distance is nominally 73 meters according to equation 4.2. This notional distance is unlikely to be realized in practice, as inhomogeneities in the beam will tend to seed the formation of individual filaments much earlier. In the approximately 0.33 meter distance of water propagation length we had available, formation of filaments from an unfocused beam was observed to occur at a distance of 12 cm propagation distance into the water. The water was enclosed in a glass tank, and slight irregularities in flat glass can also serve to seed initial inhomogeneities. In table 4.1 we give the propagation distance through water in a glass-walled tank after which filaments are observed to form, under various conditions of external focusing. For larger distances, multiple filaments and the formation of filament bundles were observed. These measurements were conducted to ensure a robust and repeatable ability to position the initial location of filamentation at a given propagation length within the water. While we did not image filaments produced by long focal length (> 5 cm) lenses, the tabulated data for these lenses shows that the perturbative processes which seed collapse and breakup are much more important than the self-focusing distance in terms of controlling the actual distance for filamentation.

Having established representative experimental parameters for beam breakup and the formation of multiple filaments, it is possible to construct an imaging apparatus for time-resolved imaging of the breakup process.

Lens focal length	Lens to glass distance	Glass to filament distance
5.0 cm	1.0 cm	1.0 cm
50.0 cm	1.0 cm	7.0 cm
50.0 cm	5.0 cm	6.0 cm
50.0 cm	10.0 cm	5.0 cm
50.0 cm	15.0 cm	3.5 cm
50.0 cm	20.0 cm	2.0 cm
50.0 cm	25.0 cm	1.0 cm
50.0 cm	31.0 cm	0.5 cm
100.0 cm	1.0 cm	11.0 cm
100.0 cm	5.0 cm	8.0 cm
100.0 cm	10.0 cm	5.0 cm
100.0 cm	15.0 cm	6.0 cm
100.0 cm	20.0 cm	5.0 cm
100.0 cm	25.0 cm	5.0 cm
100.0 cm	35.0 cm	2.0 cm
100.0 cm	40.0 cm	2.0 cm
100.0 cm	52.0 cm	1.0 cm

Table 4.1: Distances from entrance point of beam into water to point of first observed filamentation

4.3 Experimental Apparatus

In order to produce a femtosecond filament bundle along with an imaging pulse, the output of the Ti:Sapphire amplifier is directed into a beamsplitter which reflects approximately 4% of the incoming energy and transmits approximately 90% (another 4% is lost in reflection from the back surface of the beamsplitter). The transmitted pulse is directed through a 5 cm focal length positive focusing lens and directed vertically downward into an acrylic cuvette filled with water. The downward propagation direction permits the beam to enter the water without passing through the sides of the container holding the water, which removes a possible source of additional initial beam inhomogeneity. Additionally, the distance from the lens to the water surface is adjustable.

The low-intensity pulse which is reflected from the beamsplitter is directed into a corner cube retroreflector which is mounted on an electronically controllable translation stage. The imaging pulse is then directed along a path which intersects the water-filled cuvette perpendicular to the direction of propagation of the filaments. The delay between the arrival of the pulse which produces the filaments and the pulse which supplies the imaging light is controllable by appropriate translation of the stage. While the imaging pulse is required to pass through the cuvette walls and the water within the cuvette, the group velocity dispersion experienced by the pulse does not substantially lengthen it or degrade the temporal resolution. The group velocity dispersion parameter of water at 800 nanometers is $k'' = 24.76\,\mathrm{fs}^2/\mathrm{mm}$ [101]. The expression for pulse lengthening in a dispersive medium is [102]

$$\tau = \tau_0 \sqrt{1 + \left(4 \log(2) \frac{D}{\tau_0^2}\right)}, \tag{4.4}$$

where $D = k''z$ is the second-order dispersion multiplied by the propagation distance. Given the measured 10.0 mm propagation distance of the imaging pulse through the water, this will lengthen our approximately 50 femtosecond pulse to about 51.9 femtoseconds. The plastic walls of the cell are measured to be 1.14 mm thickness each, so their effect with respect to pulse lengthening will be proportionally smaller.

After passing through the cell, the imaging pulse passes through a 5 cm focal length imaging lens positioned on a translation stage between the cell and a computer-controlled CCD. The translation stage allows focusing of the region of multiple filamentation on the CCD surface at a known magnification. In this experiment the focusing lens of diameter 3.48 cm was positioned 6.5 cm from the center of the cell for a numerical aperture of 0.267. The depth of field d for a microscope in this configuration is $d = \lambda\sqrt{1+n^2}/n^2 \approx 11.5\,\mu\mathrm{m}$, which is in this case is approximately

11.5 microns. The region of multiple filamentation is comparable in size to the beam diameter, which is much larger. Sharply focusing the imaging system on every feature of interest simultaneously is not possible. However, we are primarily interested in the overall behavior of the beam as a whole as it filaments and breaks up. These filaments are distributed across the profile of the beam, and are distinguishable even when somewhat out of focus.

In this experiment we image the filamenting pulse at various depths as it propagates downward, collecting image data on its initial formation of filaments and eventual breakup.

4.4 Results

In order to characterize beam breakup and the onset of filamentation, we image the region where filaments are initially observed to form. This is possible by visual inspection of the water cell with a small amount of Rhodamine B dye dissolved in the cell. The location where filaments begin to form is evident by the visible extremely thin streaks of florescence which are visible in the cell. The cell including dye was only used to make the initial determination as to the spatial location of the filamentation. All images and extracted data in this experiment were measured in an identical cell containing distilled water without dye. For this experiment, a 5 cm focal length lens was used to focus the filament-forming pulse into the water. The 5 cm lens was positioned 3 cm from the surface of the water.

A time-resolved image of the region of the beginning of filamentation is shown in figure 4.1. In this image the pulse front has already passed out of the frame.

The small-scale filamentary structures are observed to begin well before the onset of the region of mature individual femtosecond filaments. Because of the relatively narrow depth of field of the imaging system and the much wider width of the beam

Figure 4.1: Raw background-subtracted image of refractive index changed introduced by a pulse of peak power $P \gg P_{cr}$ in liquid water, near the beginning of the filamentation region

region, precise mensuration of the filamentary structures is difficult. In order to gain insight on the formation of these structures, we collect a time-resolved image (figure 4.2) of the pulse during its propagation, when the pulse front is halfway down the frame. On the pulse front, between the filamentary region and the undisturbed area of liquid where the pulse has not yet propagated, there is a region of about 200 microns thickness of slightly mottled appearance which apparently represents a refractive index modulation lasting on the order of 0.5 picoseconds.

To gain numerical insight into the features in figure 4.2, we average over 20-pixel-wide slices in the horizontal direction and calculate the numerical Fourier transform. The first slice, its Fourier transform shown in figure 4.3, is a cut near the top of the image through the filamentary region. The second slice, its Fourier transform shown in 4.4, is a cut near the middle of the image through the mottled region. The

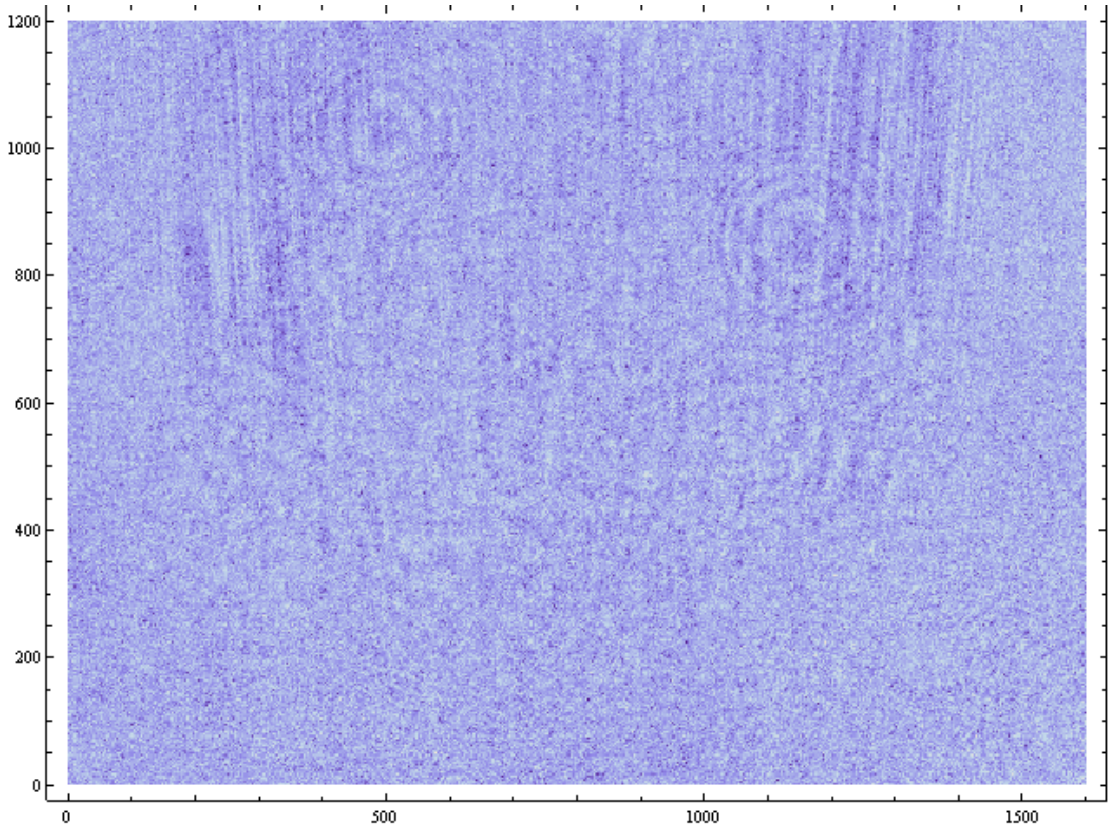

Figure 4.2: Processed image of the pulse, with pulse front propagated halfway through the frame (axis scales in microns)

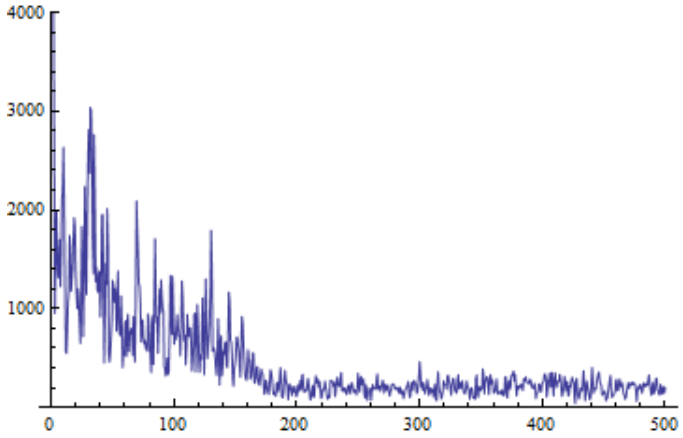

Figure 4.3: Smoothed Fourier transform of slice through filamentary region (Vertical scale arbitrary units, horizontal axis units mm^{-1})

third slice, its Fourier transform shown in 4.5, is a cut near the bottom of the image through the undisturbed region.

In figures 4.3, 4.4, and 4.5, the x-axis scale is in units of mm^{-1}. This represents the spatial frequencies of the generated features in configuration space, not the wavenumber representing the frequency of the light wave itself. In the transform of the slice representing the filamentary region (figure 4.3), the Fourier transform contains a prominent feature near 35 mm^{-1}, corresponding to a typical feature size of 28.6 microns. The Fourier transform contains significant frequency content up to a cutoff observed to occur at a spatial frequency of approximately 200 mm^{-1}, or about 5 microns. This length scale corresponds to the typical size of femtosecond laser filaments in condensed matter [17–19]. The mottled region also appears to have a spatial frequency cutoff at approximately 25 mm^{-1}, corresponding to a typical minimum feature size of 40 microns.

Interpretation of these results is complicated by the fact that the region of pulse propagation is not entirely within the focal depth and the structure within that region is not guaranteed to be identical from shot to shot due to variations in the

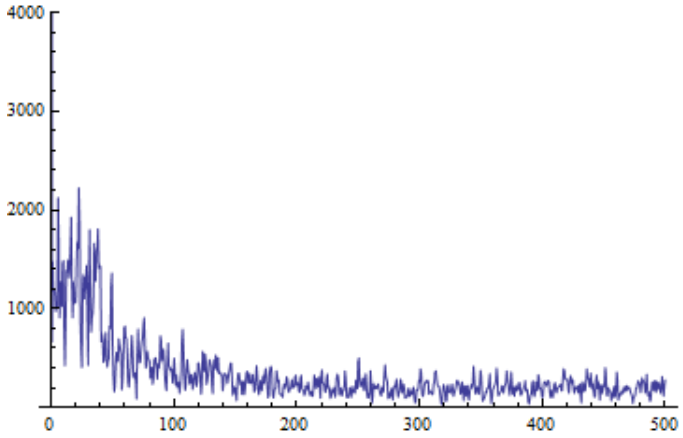

Figure 4.4: Smoothed Fourier transform of slice through mottled region (Vertical scale arbitrary units, horizontal axis units mm^{-1})

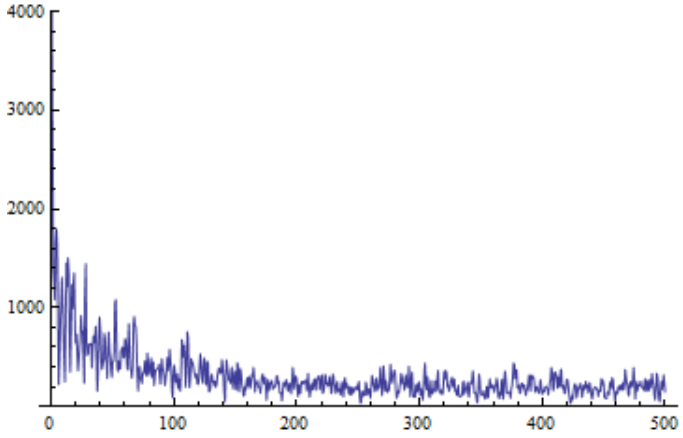

Figure 4.5: Smoothed Fourier transform of slice through empty region (Vertical scale arbitrary units, horizontal axis units mm^{-1})

pulse and the chaotic nature of the seeding process during self-focusing. However, the Fourier transform is somewhat insensitive as to whether or not a set of spatial features is in focus. The high-frequency cutoff for the spatial frequencies will still be set by those features which are in focus, which, provided the generated features are generally isotropic over the region of pulse propagation.

Below this region of beam breakup, we observe the region where the entire beam self-focused into the regime of mature multiple filamentation. The change in refractive index increases and the structure of individual filaments is apparent in the series of time-resolved images shown in figure 4.6. In each case the pulse is imaged in a time-resolved manner such that the leading edge of the pulse is approximately at the halfway point in the frame as it propagates from top to bottom.

In principle additional information about the mottled region could be extracted by time-resolved birefringence imaging as per the methods of chapter 3. However, the cell holding the liquid water is itself highly birefringent and extraction of a signal from the very strong background is experimentally challenging.

4.5 Discussion

In this chapter, we have reviewed the ultrafast imaging technique as applied to the propagation of pulses with $P \gg P_{cr}$ in a liquid medium. First, the imaging shows the presence of a large number of micron-scale filamentary plasma features which persist over at least nanosecond time scales. These features are present before the depth at which visible individual white-light-generating filaments begin to appear. They are approximately 5 microns in transverse extent, and appear throughout the volume of the pulse. At the leading area of the pulse, a mottled region with an apparent thickness of ~ 200 microns appears along the direction of propagation. Beyond this region, mature individual filaments form.

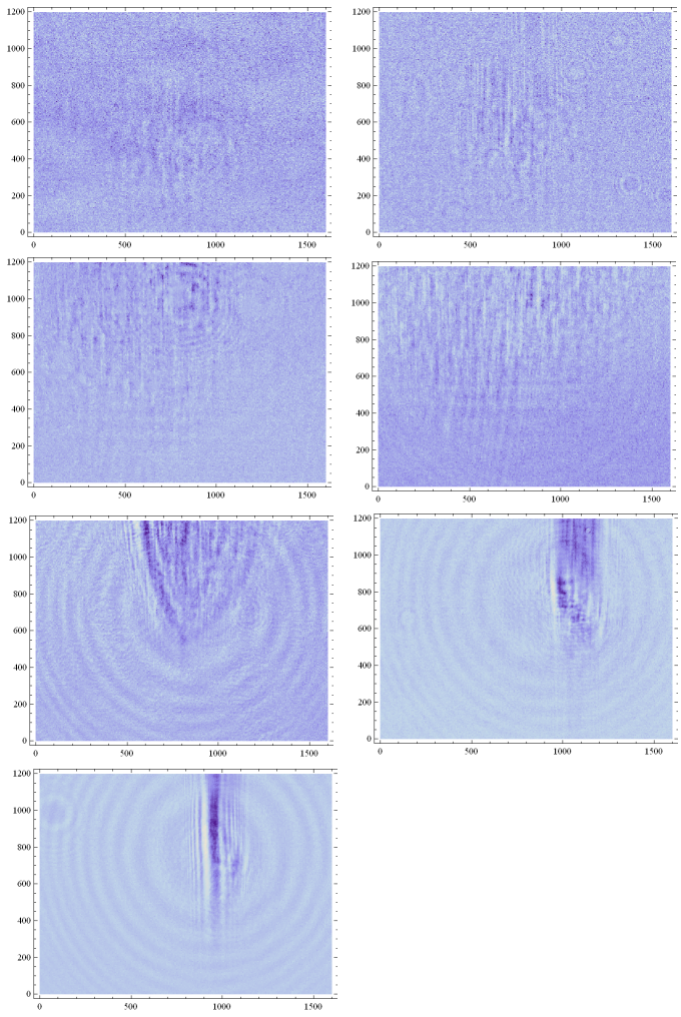

Figure 4.6: Time-resolved images of beam propagation, breakup, and filamentation. In reading order, the frames are centered at 4.44, 4.94, 12.94, 17.94, 20.94, and 22.94 mm below the water surface.

For a pulse propagating in the linear or near-linear regime, the volume of the pulse would remain relatively homogeneous during its propagation. The observation of internal structure within the pulse demonstrates the existence of structure within the pulse indicating the presence of substantial nonlinearity in the seeding process before the onset of filaments. These observations shed additional light onto the process of pulse breakup and filamentation.

5. TIME-RESOLVED PROPAGATION OF SINGLE FILAMENTS IN AIR

5.1 Introduction

The nonlinearities in a dielectric which are induced by an intense laser pulse serve to modify the refractive index. These modifications originate from different effects and span a wide range of time scales and magnitude of the associated $\Delta\tilde{n}$, both in terms of the phase shift and attenuation. Due to the high intensity, direct measurements of the pulse are difficult due to the potential for the destruction of the measuring apparatus. A few methods such as pump-probe interference experiments [103], time-resolved shadowgraphy with focused beams [82], and other techniques discussed in the literature review in sections 1.3.2 and 1.3.3.

None of these experiments produce a direct image or shadowgraph which is resolved in both the time and space domains. This has lead to a gap in the experimental characterization of filaments, as some degree of indirection has been required to extract information about the propagation of the pulse. Since filamentation is understood to be a dynamic interplay between self-focusing, plasma defocusing, self-phase modulation, pulse steepening and numerous other effects, the pulse is a dynamic object whose properties are likely to be functions of both spatial and temporal position. Direct imaging is thus a promising experimental avenue for understanding femtosecond laser filaments. In some circumstances shadowgraphy also has potential to extract information about the spatial variation in the index of refraction in nonlinear optical processes.

5.2 Diffraction Theory

From a linear systems perspective, the optical field at the object plane undergoes a linear transformation as it propagates in space or through an imaging system

such as a lens. This transformation is sometimes termed diffraction or interference according to the context, but both are fundamentally the same process [104]. Following the treatment and notation of Goodman [105] we can develop a basic theory of shadowgraphy and imaging.

In free space away from sources the spatial part of the electric field, $U(\mathbf{r})$, satisfies the Helmholtz equation

$$(\nabla^2 + k^2)U = 0. \tag{5.1}$$

Under the same conditions, the source Green's function G will also satisfy the Helmholtz equation, $(\nabla^2 + k^2)U = 0$. Given any two reasonably well-behaved functions U and G, Green's formula[1] gives a relation between the behavior of those functions on a closed surface to the behavior of the functions within the volume enclosed by that surface

$$\int_V \left(G\nabla^2 U - U\nabla^2 G\right)\, dV = \int_S \left(G\frac{\partial U}{\partial n} - U\frac{\partial G}{\partial n}\right)\, ds. \tag{5.2}$$

Now consider a small sphere S_ϵ surrounding the observation point, within a larger surface S such that the total surface is $S' = S + S_\epsilon$. Over the enclosed volume, equation 5.1 combined with equation 5.2 implies that

$$\int_V \left(G\nabla^2 U - U\nabla^2 G\right)\, dV = -\int_V \left(GUk^2 - UGk^2\right)\, dV = 0. \tag{5.3}$$

[1]This is called "Green's theorem" in many texts including [105] and [106], but it is often called Green's formula to distinguish it from the more commonly-recognized Green's theorem which establishes a relation between the integral of the curl over a plane region and the line integral over its boundary. The two theorems are related—Green's formula follows from the divergence theorem, and both the divergence theorem and Green's theorem are consequences of the more general Stokes theorem.

Thus

$$\int_{S'} \left(G\frac{\partial U}{\partial n} - U\frac{\partial G}{\partial n} \right) = 0, \tag{5.4}$$

which is equivalent to saying that

$$-\int_{S_\epsilon} \left(G\frac{\partial U}{\partial n} - U\frac{\partial G}{\partial n} \right) ds = \int_{S} \left(G\frac{\partial U}{\partial n} - U\frac{\partial G}{\partial n} \right) ds. \tag{5.5}$$

The obvious choice of the Green's function G is a diverging spherical wave,

$$G(P) = \frac{e^{ikr_{01}}}{r_{01}}. \tag{5.6}$$

This choice of Green's function leads to the Fresnel-Kirchoff formulation of scalar diffraction theory[2]. The normal derivative of this Green's function is

$$\frac{\partial G(P)}{\partial n} = \cos\left(n, r_{01}\right) \left(ik - \frac{1}{r_{01}} \right) \frac{e^{ikr_{01}}}{r_{01}}, \tag{5.7}$$

where the cosine term involves the angle between the normal vector and the line joining the observation point and the source point. If the source point is on S_ϵ, the Green's function is

$$G(P) = \frac{e^{ik\epsilon}}{\epsilon}. \tag{5.8}$$

$$\frac{\partial G(P)}{\partial n} = \frac{e^{ik\epsilon}}{\epsilon} \left(\frac{1}{\epsilon} - ik \right). \tag{5.9}$$

[2]Other Green's functions are possible. The boundary conditions involved in the Fresnel-Kirchoff formulation assume that both U and $\partial U/\partial n$ are zero on the screen surrounding the diffraction aperture, which turns out not to be mathematically consistent. The inconsistency may be formally resolved by the choice of an alternate Green's function such as in the Rayleigh-Sommerfeld formulation of diffraction. In practice the choice of formulation is rarely significant.

Thus

$$\int_{S_\epsilon} \left(G\frac{\partial U}{\partial n} - U\frac{\partial G}{\partial n} \right) = 4\pi\epsilon^2 \left[\frac{\partial G(P)}{\partial n}\frac{e^{ik\epsilon}}{\epsilon} - U(P)\frac{e^{ik\epsilon}}{\epsilon}\left(\frac{1}{\epsilon} - ik\right)\right], \tag{5.10}$$

which as $\epsilon \to 0$ gives

$$\int_{S_\epsilon} \left(G\frac{\partial U}{\partial n} - U\frac{\partial G}{\partial n} \right) = -4\pi U(P). \tag{5.11}$$

With this result and equation 5.5 in hand, this gives the Helmholtz-Kirchhoff integral theorem

$$U(P) = \frac{1}{4\pi}\int_{S_\epsilon} \left(\frac{\partial G(P)}{\partial n}\left[\frac{e^{ikr_{01}}}{r_{01}}\right] - U\frac{\partial}{\partial n}\left[\frac{e^{ikr_{01}}}{r_{01}}\right]\right) ds \tag{5.12}$$

At this point we have an expression for the field at a point P given the fields on a surface surrounding P. In diffraction theory, the choice for the surface is the plane containing the diffracting aperture and the "sphere at infinity" on the outgoing side[3]. Some manipulation and approximation involving dropping terms in $1/r_{01}$ yields the Huygens principle interpretation of diffraction,

$$U(P) = \int_A U'(P')\frac{e^{ikr_{01}}}{r_{01}}\, dA, \tag{5.13}$$

where A is the aperture and $U'(P')$ is the field incident on the aperture. Appendix A describes an interpretation of equation 5.13 in terms of the Fourier transform as well as a *Mathematica* program for evaluating it numerically.

[3]The requirement that the integral of the field on the sphere at infinity goes to zero is called the Sommerfeld radiation condition and is satisfied for physically reasonable fields.

5.3 Diffraction by Femtosecond Laser Filaments

The change in refractive index induced by an intense laser pulse in the regime of filamentation or optical breakdown comes primarily from two effects: the optical Kerr effect which generally induces an instantaneous positive change in the refractive index proportional to the intensity, and the generation of plasma which induces a negative change in the refractive index which persists as the plasma persists—generally from picoseconds to nanoseconds. In this experiment, the diffracting aperture is entirely clear with the exception of the filament itself and (when computed numerically) the sides of the window over which the integral is numerically evaluated.

For femtosecond laser filaments in air, the first relevant nonlinear quantity is the nonlinear index coefficient of about $5.0 \times 10^{19}\,\mathrm{W/cm^2}$. The typical intensity within a filament is $5.0 \times 10^{13}\,\mathrm{W/cm^2}$, yielding $\Delta n \approx 2.5 \times 10^{-5}$. The phase shift is this quantity multiplied by the ratio of the propagation length to the wavelength. Given that filaments in air are expected to be on the order of 100 microns diameter while the wavelength of the imaging light is 800 nanometers, the overall phase shift could be expect to be on the order of 3×10^{-3} radians.

With wavelength and beam diameter parameters approximately corresponding to the size of the imaging beam available in our lab, it is possible to numerically calculate the expected diffraction pattern. Assuming a 100 micron filament with the phase shift calculated above, we calculate the observed diffraction pattern shown in figure 5.1. Numerical calculation suggests that the fringe contrast in the diffraction pattern is approximately 2%, leaving this pattern almost indistinguishable by eye from the beam in the absence of a diffractiing filament. Background subtraction shown in figure 5.2 reveals the pattern, along with some calculational artifacts resulting from the finite size of the calculation window. These diffraction patterns are purely intensity

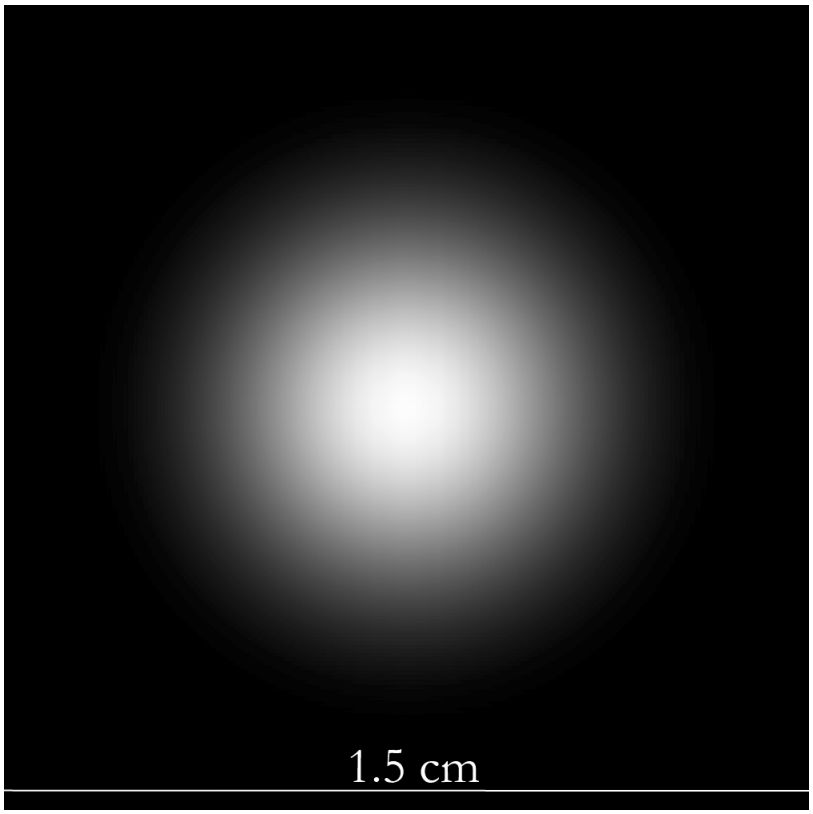

Figure 5.1: Diffraction pattern calculated for 100 micron filament with expected phase shift. The pattern is low-contrast and almost invisible without background subtraction

objects, so straightforward inversion to reveal the diffracting structure is not possible. There are a number of methods for numerical inversion of diffraction patterns in some circumstances [107, 108], but in this chapter we will use the simplest possible method—direct comparison of observed diffraction patterns to the diffraction patterns calculated for various possible filament configurations. Example calculations are shown in figure 5.3.

In this experiment, the optical filament is located a distance of 34.5 cm from the CCD beam profiler. This distance is chosen primarily for experimental convenience, but happens to span a useful range of Fresnel numbers. The Fresnel number is given

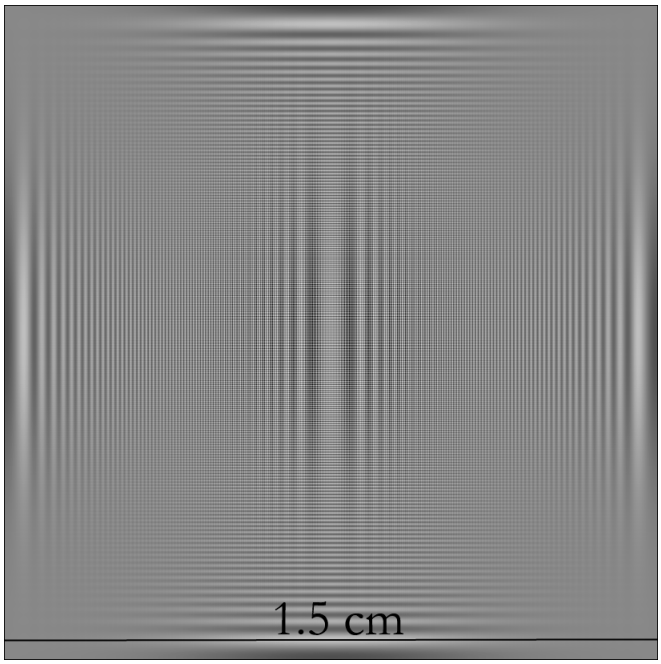

Figure 5.2: Diffraction pattern calculated for 100 micron filament with expected phase shift and background subtraction

by

$$F = \frac{a^2}{L\lambda}, \tag{5.14}$$

where a is the characterisic size of the aperture (in this case, the diameter of the filament), L is the distance from the diffracting aperture to the observation plane, and λ is the wavelength of the light. Fresnel numbers much smaller than 1 represent far-field diffraction, Fresnel numbers much larger than 1 represent ray optics, and Fresnel numbers ~ 1 are intermediate between the two. For the parameters in this experiment, a 100 micron diameter filament represents diffraction with a Fresnel number of about 0.036, while a 200 micron diameter filament has a Fresnel number of 0.144. Thus structures which are larger than expected for a filament will have diffraction patterns which increasingly resemble near-field diffraction patterns. Filaments which are smaller than the expected 100 micron diameter will all appear

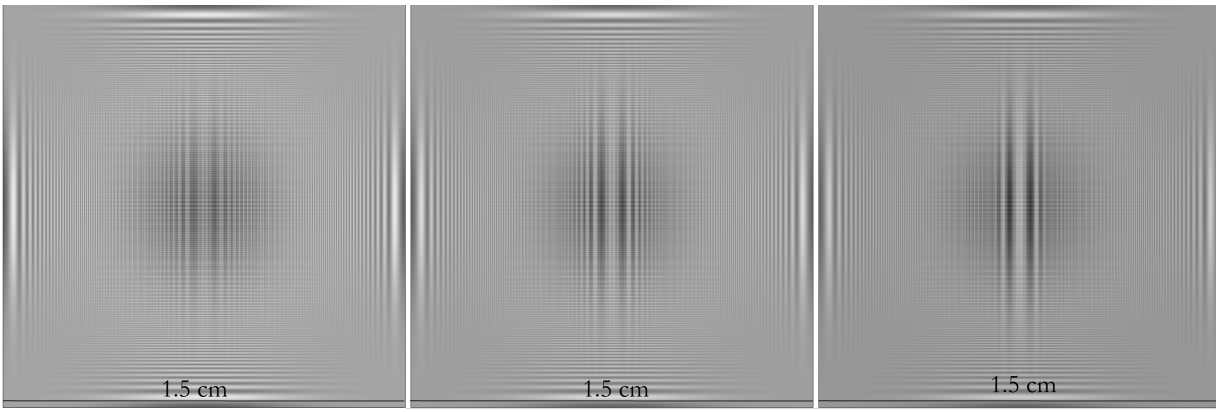

Figure 5.3: Diffraction pattern calculated for 50, 100, and 200 micron filaments (left to right) with expected phase shift and background subtraction

as far-field diffraction patterns analogous to those produced by a thin single slit[4]. These diffraction patterns reveal information about their diffracting structures both in terms of the fringe spacing and the contrast ratio which is indicative of the overall scattering cross-section.

A subtracted experimental shadowgraph is shown in figure 5.4. The filament was produced by a 1 m focal length lens with a pulse of 1.6 mJ energy.

[4]Babinet's principle states that $U_1 + U_2 = U$, where U_1 is the pattern resulting from the diffracting aperture, U_2 is the pattern resulting from the complement of the diffracting aperture, and U is the undiffracted beam. In this case it implies, as a rough intuitive picture, that a hair and an equivalently-sized slit in an opaque aperture have similar diffraction patterns.

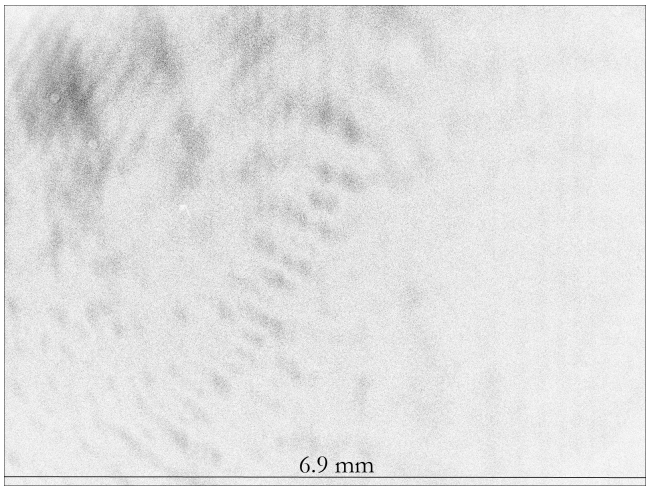

Figure 5.4: Diffraction pattern as experimentally observed from filament produced by 1 m lens

5.4 Discussion

Among the outstanding issues in filamentation physics is the dynamics of the propagation of the filament, such as the cycles of focusing and defocusing. Since this shadowgraphy technique allows relatively robust determination of filament extent and refractive index over small spatial and temporal scales, we can examine the filament over femtosecond time scales to confirm or dismiss the possibility of focusing/defocusing cycles over micron to millimeter scales. Integrating the observed background-subtracted diffraction pattern along the vertical axis to improve the contrast, we can clearly distinguish the fringes in figure 5.5. The calculated diffraction pattern for a 100 micron diameter filament of refractive index $\Delta n = 2.5 \times 10^{-5}$ shown in figure 5.2 can be integrated by the same method. The result is shown in figure 5.6. The fringe spacing, relative size, and contrast ratio are all diagnostic of the accuracy of the refractive index model corresponding to a filament of given diameter and Δn. The combined plot of the calculated and observed diffraction pattern in shown in figure 5.7. While the level of noise in the experimental plot is substantial, the overall fringe spacing and contrast ratio indicate good agreement with the simplified model

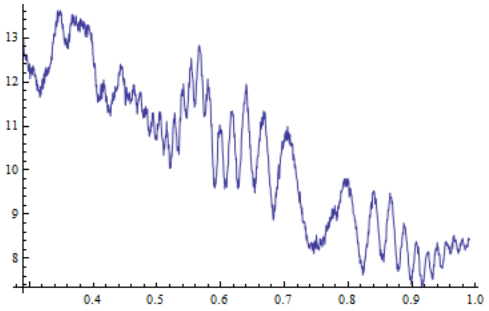

Figure 5.5: Experimentally observed diffraction pattern integrated in the vertical direction. X-axis is in cm, y-axis arbitrary intensity units

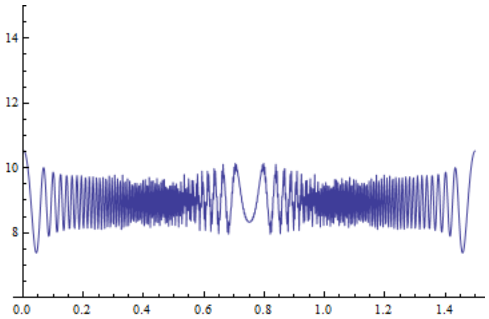

Figure 5.6: Numerically computed diffraction pattern integrated in the vertical direction. X-axis is in cm, y-axis arbitrary intensity units

of the filament refractive index.

The simplified model of the filament refractive index does not include any spatial variation on the micron to millimeter scale. If substantial variation in the filament refractive index value or the transverse spatial extent of the refractive index were present on this scale, it would be apparent in the shadowgraph. Given that such variation is not visible in the shadowgraph, variations in the filament diameter and refractive index such as may be present in the focusing/defocusing cycle are likely to only be present over much longer length scales such as the centimeter-to-meter cycles observed in the literature [63, 109].

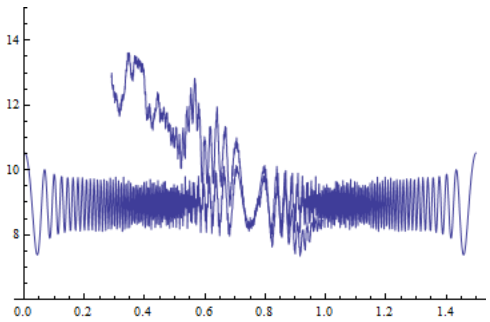

Figure 5.7: Computed and observed diffraction patterns plotted simultaneously

REFERENCES

[1] R. Boyd, *Nonlinear Optics*. Boston: Academic Press, 3 ed., 2008.

[2] J. Maxwell, "A dynamical theory of the electromagnetic field," *Philosophical Transactions of the Royal Society of London*, vol. 155, no. 1865, pp. 459–512, 1865.

[3] A. Einstein, "On the electrodynamics of moving bodies," *Annalen der Physik*, vol. 322, no. 10, pp. 891–921, 1905.

[4] A. Schawlow and C. Townes, "Infrared and optical masers," *Physical Review*, no. 2, 1958.

[5] T. Maiman, "Stimulated optical radiation in ruby," *Nature*, vol. 187, 1960.

[6] F. Byron and R. Fuller, *Mathematics of Classical and Quantum Physics*. New York: Dover, 1992.

[7] J. D. Jackson, *Classical Electrodynamics*. New York: Wiley, 3 ed., 1999.

[8] K. Oughstun and G. Sherman, *Electromagnetic Pulse Propagation in Causal Dielectrics*. Berlin: Springer-Verlag, 1994.

[9] P. Milonni and J. Eberly, *Laser Physics*. Sydney: Wiley, 2 ed., 2010.

[10] R. Chiao, E. Garmire, and C. Townes, "Self-trapping of optical beams," *Physical Review Letters*, vol. 1, no. 1, 1964.

[11] P. Kelley, "Self-focusing of optical beams," *Physical Review Letters*, no. 26, pp. 1005–1008, 1965.

[12] G. I. Stegeman, "Optical spatial solitons and their interactions: universality and diversity," *Science*, vol. 286, pp. 1518–1523, Nov. 1999.

[13] S. Chin, W. Liu, F. Théberge, Q. Luo, S. Hosseini, V. Kandidov, O. Kosareva, N. Aközbek, A. Becker, and H. Schroeder, "Some fundamental concepts of femtosecond laser filamentation," in *Progress in Ultrafast Intense Laser Science III*, ch. 12, pp. 243–264, Springer, 2008.

[14] A. Talebpour, J. Yang, and S. Chin, "Semi-empirical model for the rate of tunnel ionization of N2 and O2 molecule in an intense Ti:sapphire laser pulse," *Optics Communications*, vol. 163, pp. 29–32, May 1999.

[15] J. Kasparian, R. Sauerbrey, and S. L. Chin, "Rapid communication The critical laser intensity of self-guided light filaments in air," *Applied Physics B*, vol. 879, pp. 877–879, 2000.

[16] A. Couairon and A. Mysyrowicz, "Femtosecond filamentation in transparent media," *Physics Reports*, vol. 441, pp. 47–189, Mar. 2007.

[17] K. Yamada, W. Watanabe, T. Toma, K. Itoh, and J. Nishii, "In situ observation of photoinduced refractive-index changes in filaments formed in glasses by femtosecond laser pulses.," *Optics Letters*, vol. 26, pp. 19–21, Jan. 2001.

[18] L. Sudrie, A. Couairon, M. Franco, B. Lamouroux, B. Prade, S. Tzortzakis, and A. Mysyrowicz, "Femtosecond Laser-Induced Damage and Filamentary Propagation in Fused Silica," *Physical Review Letters*, vol. 89, p. 186601, Oct. 2002.

[19] S. Onda, W. Watanabe, K. Yamada, K. Itoh, and J. Nishii, "Study of filamentary damage in synthesized silica induced by chirped femtosecond laser pulses," *Journal of the Optical Society of America B*, vol. 22, no. 11, p. 2437, 2005.

[20] B. La Fontaine, F. Vidal, Z. Jiang, C. Y. Chien, D. Comtois, a. Desparois, T. W. Johnston, J.-C. Kieffer, H. Pepin, and H. P. Mercure, "Filamentation

of ultrashort pulse laser beams resulting from their propagation over long distances in air," *Physics of Plasmas*, vol. 6, no. 5, p. 1615, 1999.

[21] S. Tzortzakis and B. Prade, "Time-evolution of the plasma channel at the trail of a self-guided IR femtosecond laser pulse in air," *Optics Communications*, vol. 181, no. July, pp. 123–127, 2000.

[22] A. Talebpour, M. Abdel-Fattah, and S. Chin, "Focusing limits of intense ultrafast laser pulses in a high pressure gas: road to new spectroscopic source," *Optics communications*, no. September, pp. 479–484, 2000.

[23] S. Chin, *Femtosecond Laser Filamentation*. Springer, 2010.

[24] G. Méchain, Y.-B. André, S. Tzortzakis, M. Franco, B. Prade, A. Mysyrowicz, A. Couairon, E. Salmon, and R. Sauerbrey, "Range of plasma filaments created in air by a multi-terawatt femtosecond laser," *Optics Communications*, vol. 247, pp. 171–180, Mar. 2005.

[25] O. G. Kosareva, V. P. Kandidov, A. Brodeur, C. Y. Chien, and S. L. Chin, "Conical emission from laser plasma interactions in the filamentation of powerful ultrashort laser pulses in air.," *Optics Letters*, vol. 22, pp. 1332–4, Sept. 1997.

[26] J. Kasparian, M. Rodriguez, G. Méjean, J. Yu, E. Salmon, H. Wille, R. Bourayou, S. Frey, Y. B. Andre, a. Mysyrowicz, R. Sauerbrey, J. P. Wolf, and L. Wöste, "White-light filaments for atmospheric analysis.," *Science (New York, N.Y.)*, vol. 301, pp. 61–4, July 2003.

[27] A. Sommerfeld, "About the propagation of light in dispersive media," *Annals of Physics*, vol. 44, 1914.

[28] L. Brillouin, "Light diffusion by a homogeneous transparent body," *Comptes Rendus Hebdomadaires des Seances de lAcademie des Sciences*, 1914.

[29] K. Oughstun and G. Sherman, "Electromagnetic Pulse Propagation in Causal Dielectrics," *IEEE Antennas and Propagation Magazine*, vol. 79, no. 9102509, 1996.

[30] K. Oughstun and G. Sherman, "Propagation of electromagnetic pulses in a linear dispersive medium with absorption (the Lorentz medium)," *Journal of the Optical Society of America B*, vol. 5, no. 4, 1988.

[31] P. Pleshko and I. Palócz, "Experimental observation of Sommerfeld and Brillouin precursors in the microwave domain," *Physical Review Letters*, vol. 22, no. 22, 1969.

[32] O. Avenel, M. Rouff, E. Varoquaux, and G. Williams, "Resonant Pulse Propagation of Sound in Superfluidˆ{3} He-B," *Physical Review Letters*, vol. 50, no. 20, pp. 1591–1594, 1983.

[33] H. Jeong, A. M. C. Dawes, and D. J. Gauthier, "Direct Observation of Optical Precursors in a Region of Anomalous Dispersion," *Physical Review Letters*, vol. 96, p. 143901, Apr. 2006.

[34] J. F. Chen, S. Wang, D. Wei, M. M. T. Loy, G. K. L. Wong, and S. Du, "Optical coherent transients in cold atoms: From free-induction decay to optical precursors," *Physical Review A*, vol. 81, p. 033844, Mar. 2010.

[35] B. Macke and B. Ségard, "Optical precursors in transparent media," *Physical Review A*, vol. 80, p. 011803, July 2009.

[36] J. Chen, M. Loy, and H. Jeong, *Optical Precursors: From Classical Waves to Single Photons*. New York: Springer, 2013.

[37] J. Aaviksoo, J. Kuhl, and K. Ploog, "Observation of optical precursors at pulse propagation in GaAs," *Physical Review A*, pp. 5353–5356, 1991.

[38] T. Roberts, "Comment on Observation of Optical Precursors in Water," *Physical Review Letters*, vol. 93, p. 269401, Dec. 2004.

[39] R. Alfano, J. Birman, X. Ni, M. Alrubaiee, and B. Das, "Comment on Observation of Optical Precursors in Water," *Physical Review Letters*, vol. 94, p. 239401, June 2005.

[40] L. Naveira, B. Strycker, and J. Wang, "Propagation of femtosecond laser pulses through water in the linear absorption regime," *Applied Optics*, vol. 48, pp. 1828–36, Apr. 2009.

[41] A. Sokolov, L. Naveira, and M. Poudel, "Propagation of ultrashort laser pulses in water: linear absorption and onset of nonlinear spectral transformation.," *Applied Optics*, vol. 49, pp. 513–9, Jan. 2010.

[42] M. M. Springer, W. Yang, A. A. Kolomenski, H. A. Schuessler, J. Strohaber, G. W. Kattawar, and A. V. Sokolov, "Observation of precursorlike behavior of femtosecond pulses in a dye with a strong absorption band," *Physical Review A*, vol. 83, pp. 1–6, Apr. 2011.

[43] R. Chiao, M. Johnson, S. Krinsky, H. Smith, and C. Townes, "A New Class of Trapped Light Filaments," *IEEE Journal of Quantum Electronics*, no. 9, pp. 467–469, 1966.

[44] J. Marburger, "Self-focusing: Theory," *Progress in Quantum Electronics*, vol. 4, 1975.

[45] Y. Shen, "Self-focusing: Experimental," *Progress in Quantum Electronics*, vol. 4, pp. 1–34, Apr. 1975.

[46] A. Braun, G. Korn, X. Liu, D. Du, J. Squier, and G. Mourou, "Self-channeling of high-peak-power femtosecond laser pulses in air," *Optics Letters*, vol. 20, pp. 73–5, Jan. 1995.

[47] E. T. Nibbering, P. F. Curley, G. Grillon, B. S. Prade, M. A. Franco, F. Salin, and A. Mysyrowicz, "Conical emission from self-guided femtosecond pulses in air.," *Optics Letters*, vol. 21, pp. 62–5, Jan. 1996.

[48] R. Trebino, *Frequency-Resolved Optical Gating: The Measurement of Ultrashort Laser Pulses*. Springer, 2002.

[49] Q. Feng, J. Moloney, A. C. Newell, E. Wright, K. Cook, P. Kennedy, D. Hammer, B. Rockwell, and C. Thompson, "Theory and simulation on the threshold of water breakdown induced by focused ultrashort laser pulses," *IEEE Journal of Quantum Electronics*, vol. 33, no. 2, pp. 127–137, 1997.

[50] N. Tang and R. L. Sutherland, "Time-domain theory for pumpprobe experiments with chirped pulses," *Journal of the Optical Society of America B*, vol. 14, p. 3412, Dec. 1997.

[51] D. Du, X. Liu, G. Korn, J. Squier, and G. Mourou, "Laser-induced breakdown by impact ionization in SiO2 with pulse widths from 7 ns to 150 fs," *Applied Physics Letters*, vol. 64, no. 23, p. 3071, 1994.

[52] K. M. Davis, K. Miura, N. Sugimoto, and K. Hirao, "Writing waveguides in glass with a femtosecond laser.," *Optics Letters*, vol. 21, pp. 1729–31, Nov. 1996.

[53] A. Couairon, L. Sudrie, M. Franco, B. Prade, and A. Mysyrowicz, "Filamentation and damage in fused silica induced by tightly focused femtosecond laser pulses," *Physical Review B*, vol. 71, p. 125435, Mar. 2005.

[54] H. R. Lange, G. Grillon, J. F. Ripoche, M. A. Franco, B. Lamouroux, B. S. Prade, A. Mysyrowicz, E. T. Nibbering, and A. Chiron, "Anomalous long-range propagation of femtosecond laser pulses through air: moving focus or pulse self-guiding?," *Optics Letters*, vol. 23, pp. 120–2, Jan. 1998.

[55] W. Liu, O. Kosareva, I. Golubtsov, A. Iwasaki, A. Becker, V. Kandidov, and S. Chin, "Random deflection of the white light beam during self-focusing and filamentation of a femtosecond laser pulse in water," *Applied Physics B: Lasers and Optics*, vol. 75, pp. 595–599, Oct. 2002.

[56] A. Dubietis, G. Tamosauskas, I. Diomin, and A. Varanavicius, "Self-guided propagation of femtosecond light pulses in water.," *Optics Letters*, vol. 28, pp. 1269–71, July 2003.

[57] A. Matijosius, J. Trull, P. Di Trapani, A. Dubietis, R. Piskarskas, A. Varanavicius, and A. Piskarskas, "Nonlinear space-time dynamics of ultrashort wave packets in water.," *Optics Letters*, vol. 29, pp. 1123–5, May 2004.

[58] Z.-q. Hao, J. Zhang, X. Lu, T.-t. Xi, Y.-t. Li, X.-h. Yuan, Z.-y. Zheng, Z.-h. Wang, W.-j. Ling, and Z.-y. Wei, "Spatial evolution of multiple filaments in air induced by femtosecond laser pulses," *Optics Express*, vol. 14, no. 2, pp. 773–778, 2006.

[59] P. Bejot, L. Bonacina, J. Extermann, M. Moret, J. P. Wolf, R. Ackermann, N. Lascoux, R. Salame, E. Salmon, J. Kasparian, L. Berge, S. Champeaux, C. Guet, N. Blanchot, O. Bonville, A. Boscheron, P. Canal, M. Castaldi, O. Hartmann, C. Lepage, L. Marmande, E. Mazataud, G. Mennerat, L. Patissou, V. Prevot, D. Raffestin, and J. Ribolzi, "32 TW atmospheric white-light laser," *Applied Physics Letters*, vol. 90, no. 15, p. 151106, 2007.

[60] Z. Hao, J. Zhang, Z. Zhang, X. Yuan, Z. Zheng, X. Lu, Z. Jin, Z. Wang, J. Zhong, and Y. Liu, "Characteristics of multiple filaments generated by femtosecond laser pulses in air: Prefocused versus free propagation," *Physical Review E*, vol. 74, p. 066402, Dec. 2006.

[61] E. Schulz, D. S. Steingrube, T. Binhammer, M. B. Gaarde, A. Couairon, and U. Morgner, "Tracking spectral shapes and temporal dynamics along a femtosecond filament," *Optics Express*, vol. 19, no. 20, pp. 19495–19507, 2011.

[62] W. Liu, O. Kosareva, I. Golubtsov, A. Iwasaki, A. Becker, V. Kandidov, and S. Chin, "Femtosecond laser pulse filamentation versus optical breakdown in H 2 O," *Applied Physics B: Lasers and Optics*, vol. 76, pp. 215–229, Mar. 2003.

[63] W. Liu, "Multiple refocusing of a femtosecond laser pulse in a dispersive liquid (methanol)," *Optics Communications*, vol. 225, pp. 193–209, Sept. 2003.

[64] W. Liu, Q. Luo, and S. Chin, "Competition between multiphoton/tunnel ionization and filamentation induced by powerful femtosecond laser pulses in air," *Chinese Optics Letters*, vol. 1, no. 1, 2003.

[65] P. Kiran, S. Bagchi, S. Krishnan, C. Arnold, G. Kumar, and A. Couairon, "Focal dynamics of multiple filaments: Microscopic imaging and reconstruction," *Physical Review A*, vol. 82, pp. 1–8, July 2010.

[66] N. Nguyen, A. Saliminia, W. Liu, S. Chin, and R. Vallée, "Optical breakdown versus filamentation in fused silica by use of femtosecond infrared laser pulses," *Optics Letters*, vol. 28, no. 17, pp. 1591–1593, 2003.

[67] F. Théberge, W. Liu, P. Simard, A. Becker, and S. Chin, "Plasma density inside a femtosecond laser filament in air: Strong dependence on external focusing," *Physical Review E*, vol. 74, pp. 1–7, Sept. 2006.

[68] J. Yu, D. Mondelain, J. Kasparian, E. Salmon, S. Geffroy, C. Favre, V. Boutou, and J.-P. Wolf, "Sonographic probing of laser filaments in air.," *Applied Optics*, vol. 42, pp. 7117–20, Dec. 2003.

[69] A. Bernstein, M. McCormick, G. Dyer, J. Sanders, and T. Ditmire, "Two-beam coupling between filament-forming beams in air," *Physical Review Letters*, vol. 102, pp. 1–4, Mar. 2009.

[70] J. Wu, Y. Tong, X. Yang, H. Cai, P. Lu, H. Pan, and H. Zeng, "Interaction of two parallel femtosecond filaments at different wavelengths in air.," *Optics Letters*, vol. 34, pp. 3211–3, Oct. 2009.

[71] B. Strycker, M. Springer, C. Trendafilova, X. Hua, M. Zhi, A. Kolomenskii, H. Schroeder, J. Strohaber, H. Schuessler, G. Kattawar, and A. Sokolov, "Energy transfer between laser filaments in liquid methanol.," *Optics Letters*, vol. 37, pp. 16–8, Jan. 2012.

[72] A. Vogel, S. Busch, and U. Parlitz, "Shock wave emission and cavitation bubble generation by picosecond and nanosecond optical breakdown in water," *Journal of the Acoustical Society of America*, vol. 100, no. 1, pp. 148–165, 1996.

[73] L. Berthe, R. Fabbro, P. Peyre, L. Tollier, and E. Bartnicki, "Shock waves from a water-confined laser-generated plasma," *Journal of Applied Physics*, vol. 82, no. 6, p. 2826, 1997.

[74] E. N. Glezer, C. B. Schaffer, N. Nishimura, and E. Mazur, "Minimally disruptive laser-induced breakdown in water.," *Optics Letters*, vol. 22, pp. 1817–9, Dec. 1997.

[75] Y. Li, J. Zhang, H. Teng, K. Li, X. Peng, Z. Jin, X. Lu, Z. Zheng, and Q. Yu, "Blast waves produced by interactions of femtosecond laser pulses with water,"

Physical Review E, vol. 67, pp. 1–5, May 2003.

[76] C. Schaffer, N. Nishimura, E. Glezer, A. Kim, and E. Mazur, "Dynamics of femtosecond laser-induced breakdown in water from femtoseconds to microseconds.," *Optics Express*, vol. 10, pp. 196–203, Feb. 2002.

[77] M. Fujimoto, S. Aoshima, M. Hosoda, and Y. Tsuchiya, "Femtosecond time-resolved optical polarigraphy: imaging of the propagation dynamics of intense light in a medium.," *Optics Letters*, vol. 24, pp. 850–2, June 1999.

[78] M. Fujimoto, S.-i. Aoshima, M. Hosoda, and Y. Tsuchiya, "Analysis of instantaneous profiles of intense femtosecond optical pulses propagating in helium gas measured by using femtosecond time-resolved optical polarigraphy," *Physical Review A*, vol. 64, pp. 1–11, Aug. 2001.

[79] M. Fujimoto, S. Aoshima, and Y. Tsuchiya, "Multiframe observation of an intense femtosecond optical pulse propagating in air," *Optics Letters*, vol. 27, no. 5, pp. 309–311, 2002.

[80] E. Abraham, K. Minoshima, and H. Matsumoto, "Femtosecond laser-induced breakdown in water: Time-resolved shadow imaging and two-color interferometric imaging," *Optics Communications*, vol. 176, pp. 441–452, May 2000.

[81] P. Rambo, J. Schwarz, and J. Diels, "Interferometry with two-dimensional spatial and high temporal resolution," *Optics Communications*, vol. 197, no. September, pp. 145–159, 2001.

[82] G. Rodriguez, A. R. Valenzuela, B. Yellampalle, M. J. Schmitt, and K.-Y. Kim, "In-line holographic imaging and electron density extraction of ultrafast ionized air filaments," *Journal of the Optical Society of America B*, vol. 25, p. 1988, Nov. 2008.

[83] T. Balciunas, A. Melninkaitis, G. Tamosauskas, and V. Sirutkaitis, "Time-resolved off-axis digital holography for characterization of ultrafast phenomena in water.," *Optics Letters*, vol. 33, pp. 58–60, Jan. 2008.

[84] S. Minardi, A. Gopal, M. Tatarakis, A. Couairon, G. Tamosauskas, R. Piskarskas, A. Dubietis, and P. Di Trapani, "Time-resolved refractive index and absorption mapping of light-plasma filaments in water.," *Optics Letters*, vol. 33, pp. 86–8, Jan. 2008.

[85] S. Minardi, A. Gopal, A. Couairon, G. Tamoasuskas, R. Piskarskas, A. Dubietis, and P. Di Trapani, "Accurate retrieval of pulse-splitting dynamics of a femtosecond filament in water by time-resolved shadowgraphy.," *Optics Letters*, vol. 34, pp. 3020–2, Oct. 2009.

[86] X. Mao, S. S. Mao, and R. E. Russo, "Imaging femtosecond laser-induced electronic excitation in glass," *Applied Physics Letters*, vol. 82, no. 5, p. 697, 2003.

[87] J. Liu, Z. Duan, Z. Zeng, X. Xie, Y. Deng, R. Li, Z. Xu, and S. Chin, "Time-resolved investigation of low-density plasma channels produced by a kilohertz femtosecond laser in air," *Physical Review E*, vol. 72, p. 026412, Aug. 2005.

[88] Y. Hayasaki, M. Isaka, A. Takita, and S. Juodkazis, "Time-resolved interferometry of femtosecond-laser-induced processes under tight focusing and close-to-optical breakdown inside borosilicate glass.," *Optics Express*, vol. 19, pp. 5725–34, Mar. 2011.

[89] W. Gawelda, D. Puerto, J. Siegel, a. Ferrer, a. Ruiz de la Cruz, H. Fernandez, and J. Solis, "Ultrafast imaging of transient electronic plasmas produced in conditions of femtosecond waveguide writing in dielectrics," *Applied Physics Letters*, vol. 93, no. 12, p. 121109, 2008.

[90] D. G. Papazoglou and S. Tzortzakis, "In-line holography for the characterization of ultrafast laser filamentation in transparent media," *Applied Physics Letters*, vol. 93, no. 4, p. 041120, 2008.

[91] X.-L. Liu, X. Lu, X. Liu, T.-T. Xi, F. Liu, J.-L. Ma, and J. Zhang, "Tightly focused femtosecond laser pulse in air: from filamentation to breakdown.," *Optics Express*, vol. 18, pp. 26007–17, Dec. 2010.

[92] L. Yan, X. Wang, J. Si, S. Matsuo, T. Chen, W. Tan, F. Chen, and X. Hou, "Time-resolved single-shot imaging of femtosecond laser induced filaments using supercontinuum and optical polarigraphy," *Applied Physics Letters*, vol. 100, no. 11, p. 111107, 2012.

[93] U. Österberg, D. Andersson, and M. Lisak, "On precursor propagation in linear dielectrics," *Optics Communications*, vol. 277, pp. 5–13, Sept. 2007.

[94] S.-H. Choi and U. Österberg, "Observation of Optical Precursors in Water," *Physical Review Letters*, vol. 92, p. 193903, May 2004.

[95] W. Yang, M. Springer, J. Strohaber, A. Kolomenski, H. Schuessler, G. Kattawar, and A. Sokolov, "Spectral phase retrieval from interferometric autocorrelation by a combination of graduated optimization and genetic algorithms.," *Optics express*, vol. 18, pp. 15028–38, July 2010.

[96] M. Centurion, Y. Pu, Z. Liu, D. Psaltis, and T. W. Hänsch, "Holographic recording of laser-induced plasma.," *Optics Letters*, vol. 29, pp. 772–4, Apr. 2004.

[97] A. Couairon and A. Mysyrowicz, *Self-focusing: Past and Present*, vol. 114 of *Topics in Applied Physics*. New York: Springer, 2009.

[98] Y. E. Geints, A. M. Kabanov, A. A. Zemlyanov, E. E. Bykova, O. A. Bukin, and S. S. Golik, "Kerr-driven nonlinear refractive index of air at 800 and 400 nm measured through femtosecond laser pulse filamentation," *Applied Physics Letters*, vol. 99, no. 18, p. 181114, 2011.

[99] O. G. Kosareva, W. Liu, N. A. Panov, J. Bernhardt, Z. Ji, M. Sharifi, R. Li, Z. Xu, J. Liu, Z. Wang, J. Ju, X. Lu, Y. Jiang, Y. Leng, X. Liang, V. P. Kandidov, and S. L. Chin, "Can we reach very high intensity in air with femtosecond PW laser pulses?," *Laser Physics*, vol. 19, pp. 1776–1792, July 2009.

[100] V. P. Kandidov, S. A. Shlenov, and O. G. Kosareva, "Filamentation of high-power femtosecond laser radiation," *Quantum Electronics*, vol. 39, pp. 205–228, Mar. 2009.

[101] Y. Coello, B. Xu, T. Miller, V. Lozovoy, and M. Dantus, "Group-velocity dispersion measurements of water, seawater, and ocular components using multiphoton intrapulse interference phase scan," *Applied Optics*, vol. 46, no. 35, 2007.

[102] A. Weiner, *Ultrafast Optics*. Hoboken: Wiley, 2009.

[103] H. Dachraoui, C. Oberer, M. Michelswirth, and U. Heinzmann, "Direct time-domain observation of laser pulse filaments in transparent media," *Physical Review A*, vol. 82, p. 043820, Oct. 2010.

[104] R. Feynman, *The Feynman Lectures on Physics*. New York: Basic Books, 2006.

[105] J. W. Goodman, *Introduction to Fourier Optics*. New York: McGraw-Hill, 1968.

[106] M. Born and E. Wolf, *Principles of Optics*. London: Oxford University Press, 7 ed., 1999.

[107] D. Sayre, "Some implications of a theorem due to Shannon," *Acta Crystallographica*, vol. 5, 1952.

[108] S. Marchesini, H. Chapman, S. Hau-Riege, R. London, A. Szoke, H. He, M. Howells, H. Padmore, R. Rosen, J. Spence, and U. Weierstall, "Coherent X-ray Diffractive Imaging; applications and limitations," *Optics Express*, vol. 11, p. 2344, 2003.

[109] H. Wang, C. Fan, P. Zhang, C. Qiao, J. Zhang, and H. Ma, "Light filaments with higher-order Kerr effect.," *Optics Express*, vol. 18, pp. 24301–6, Nov. 2010.

APPENDIX A

MATHEMATICA CODE FOR DIFFRACTION PATTERN CALCULATIONS

A.1 Derivation

Following the notation of [105], a diffraction pattern is a result of the superposition of Huygens wavelets originating in the plane of diffraction,

$$U(x,y) = \frac{1}{i\lambda}\int_S U'(x',y')\frac{e^{ikr}}{r}\cos(n,r)\,ds, \tag{A.1}$$

where the unprimed coordinates are the coordinates of the observation points in the measurement plane, the primed coordinates are those of the points in the plane of the diffracting aperture, r is the distance between those two points, and $\cos(n,r)$ is the cosine of the angle between r and the aperture plane. U' is the field incident on the aperture and U is the field at the observation point. The integral is taken over the entire aperture plane, but is equal to 0 everywhere on that plane except for the aperture itself.

Provided the diffraction angles are not too large, we may approximate $\cos(n,r) \cong 1$ and $e^{ikr}/r \cong e^{ikr}/z$. If we also expand r in series and keep only the first two terms, we have

$$r \cong z\left(1 + \frac{1}{2}\left(\frac{x-x'}{z}\right)^2 + \frac{1}{2}\left(\frac{y-y'}{z}\right)^2\right), \tag{A.2}$$

which is the Fresnel approximation. Plugging these approximations into equation A.1 yields

$$U(x,y) = \frac{e^{ikz}}{i\lambda z}\int_S U'(x',y')\exp\left(i\frac{k}{2z}\left[(x-x')^2 + (y-y')^2\right]\right)dx'\,dy'. \tag{A.3}$$

By expanding the squared terms this can be rewritten as

$$U(x,y) = \frac{e^{ikz}}{i\lambda z} e^{i\frac{k}{2z}(x^2+y^2)} \int_S U'(x',y') e^{i\frac{k}{2z}(x'^2+y'^2)} e^{-i\frac{2\pi}{\lambda z}(x'x+y'y)}\, dx'\, dy'. \tag{A.4}$$

This equation has a convenient interpretation—up to amplitude and phase normalization factors, it is the Fourier transform of $U(x',y')\exp\left[i(k/2z)(x'^2+y'^2)\right]$. The "frequencies" in this transform are properly scaled with respect to the observation plane coordinates when $f_x = x'/\lambda z$, $f_y = y'/\lambda z$.

This Fourier transform involves very rapidly varying phases and direct integration is extremely difficult numerically. A much faster way to numerically evaluate the Fourier transform is to sample the points in the aperture plane and perform a numerical fast Fourier transform. By the scaling condition above, a wider sampling window in the observation plane leads to more closely spaced samples in the aperture plane and vice versa. Thus, increasing one of the linear dimensions of the sampling window leads to a linear increase of the density of sampling points along that dimension, which is a quadratic increase in the number of points. A linear increase in both the dimensions of the sampling window thus leads to a fourth-power increase in the number of sampled points. This rapid increase in the number of sample points is a potential area of concern during numerical evaluation of the sample points for a given field configuration and the subsequent FFT.

A.2 Code

The code for the program follows. In this case the electrical field which is being sampled is a Gaussian beam intersecting a 20 micron opaque fiber which extends halfway down the window. The final line is the command to display the resulting plot, shown in figure A.1.

```
(* all units in meters *)
```

```
\[Lambda] = 800.0 10^-9;
beamradius = 0.0046‘;
(*
z = distance to camera;
\[CapitalDelta]x = size of region to image (both in object and image \
planes);
*)
z = 0.28;
\[CapitalDelta]x = \[CapitalDelta]y = 0.015;
n = If[Mod[Floor[\[CapitalDelta]x^2/(\[Lambda] z)], 2] == 0,
   Floor[\[CapitalDelta]x^2/(\[Lambda] z)],
   Floor[\[CapitalDelta]x^2/(\[Lambda] z)] + 1];
Print["n = ", n, "\n", "\!\(\*SuperscriptBox[\(n\), \(2\)]\) = ", n^2]
Print["Step size is ", 10^6 \[CapitalDelta]x/n, " microns"]
efield = Compile[{x, y},
   Exp[(-(x/beamradius)^2) + (-(y/beamradius)^2)] (UnitStep[x])];
(* i,j runs from negative numbers to positive ones;
table1 is table which gets FFTd; *)
cf = Compile[{\[CapitalDelta]x, \[CapitalDelta]y, n, \[Lambda], z},
   table1 = Table[
      efield[(i \[CapitalDelta]x)/n, (j \[CapitalDelta]y)/n] Exp[
        I \[Pi] (\[CapitalDelta]x^2/(\[Lambda] z n^2) i^2) +
         I \[Pi] (\[CapitalDelta]y^2/(\[Lambda] z n^2) j^2)],
      {i, -n/2, n/2}, {j, -n/2, n/2}];];
TimeConstrained[
  cf[\[CapitalDelta]x, \[CapitalDelta]y, n, \[Lambda], z],
  1200] // Timing
table2 = Abs[Fourier[table1]]^2;
plotTable2 = Transpose[Reverse[RotateRight[table2, {n/2, n/2}]]];
plot2 = ArrayPlot[Max[plotTable2] - plotTable2,
     PlotRange -> {0, Max[plotTable2]}, PixelConstrained -> 1];
plot2
```

A.3 Comments on Code Operation

Computational algorithms are usually assessed in terms of their computational complexity. One classical set of examples are algorithms for sorting a list. An algorithm which sorts by randomly shuffling a list of length n and checking to see if the result is sorted has an average run time given by the product of $n!$ (the number of permutations of the list) and n, the time required to check to see if the resulting permuted list is sorted. This sort is thus $O(n \cdot n!)$ using the Landau[1] "big O" notation. One sorting algorithm commonly performed by humans who are sorting a

[1]The German mathematician Edmund Landau (1877-1938), not the Russian physicist Lev Landau.

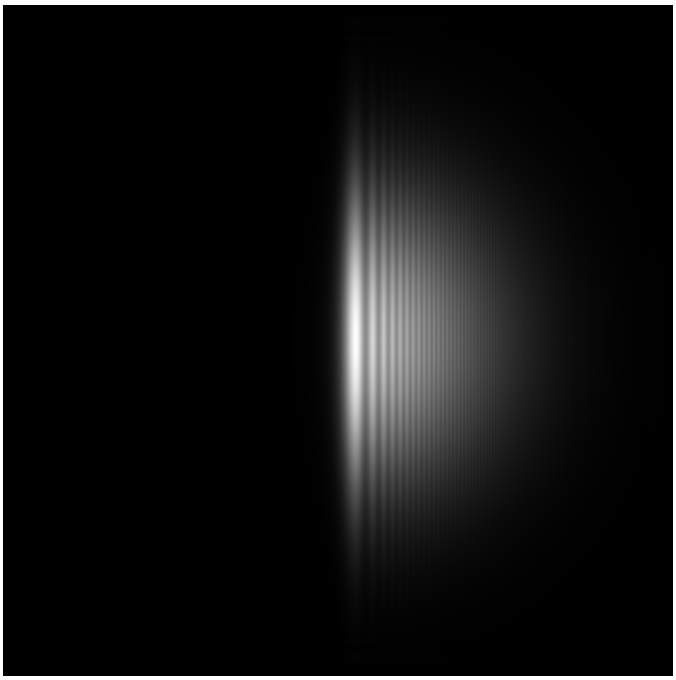

Figure A.1: Output of the program: a knife-edge blocking one half of a Gaussian beam.

list manually is the selection sort, in which the list is searched for its lowest element, that element is moved to the front of the list, and the process is repeated for the remaining unsorted list. The search of n elements is performed n times (constant factors are ignored in Landau notation) and the soring process is thus $O(n^2)$ in terms of the total number of operations required. The best possible average-case comparison sort algorithms operate in $O(n \log n)$ time[2]. These are usually implemented in computers.

The program described in this appendix is explicitly constructed such that the window size and density of sampling points are identical in both the plane of diffrac-

[2]Handwaving proof: a list may be ordered in $n!$ possible ways. Therefore $\log_2 n!$ bits are required to specify the ordering of a list. Each comparison of two elements gives 1 bit of information—is this element greater than that element, or not? By Stirling's approximation, $\log n! \sim n \log n$. Thus after dropping constant factors, $n \log n$ bits are required, and $O(n \log n)$ comparisons are required.

tion and the plane of observation. As discussed in section A.1, this requires the density of sampling points per length to scale linearly with the length itself. Thus increasing the area of the sampled region and the density of sampling points per area grow quadratically with the length of the sides of the window. The growth of the total number of points is therefore $O(L^4)$. The fast Fourier transform as implemented in Mathematica is $O(n \log n)$, so the overall scaling of the run time of the program is $O(L^4 \log L)$. A doubling of the length of the sides of the window thus increases overall run time by more than a factor of 16. Is is advisable to choose a window size and diffraction distance z such that the total number of points is tractable given the available computing power. On the author's laptop with an Intel Core i5-2450M CPU, the maximum reasonable number of points is on the order of 10^7 provided that the run time is required to be less than tens of minutes.